



## Full length article

## Energetic, structural and mechanical properties of terraced interfaces

M. Dodaran <sup>a</sup>, J. Wang <sup>b</sup>, Y. Chen <sup>c</sup>, W.J. Meng <sup>a</sup>, S. Shao <sup>a,\*</sup><sup>a</sup> Department of Mechanical and Industrial Engineering, Louisiana State University, Baton Rouge, LA, 70803, USA<sup>b</sup> Department of Mechanical and Materials Engineering, University of Nebraska-Lincoln, Lincoln, NE, 68588, USA<sup>c</sup> Department of Mechanical Engineering and Engineering Science, University of North Carolina-Charlotte, NC, 28223, USA

## ARTICLE INFO

## Article history:

Received 2 January 2019

Received in revised form

24 March 2019

Accepted 8 April 2019

Available online 11 April 2019

## Keywords:

Semi-coherent interfaces

Disconnections

Misfit dislocations

Mechanical response

Interface energy

## ABSTRACT

Taking the well-understood Cu-Ni {111} semi-coherent interface as a prototype, we demonstrate an important, yet long-been-overlooked, size effect on the properties of terraced interfaces — i.e. the facet length scale effect. Interfacial facets are considered as super interface disconnections (SIDs). We then studied the SID's size effect on the energy, structure, and mechanical response of terraced interfaces by using atomistic simulations and defect theories. We found that the specific facet energy — therefore the specific energy of the terraced interface — exhibits a periodic change with the SID's size. The periodic change is associated with the quantized transitions in their dislocation structures. Correspondingly, the mechanical response of terraced interfaces also exhibits clear regime shifts, as reflected in changes in the nucleation and emission mechanisms for lattice dislocations.

© 2019 Acta Materialia Inc. Published by Elsevier Ltd. All rights reserved.

## 1. Introduction

A solid-solid variant of the terraced surfaces — referred in this work exclusively as “terraced interfaces”— forms between similar or dissimilar crystals as grain boundaries or phase boundaries. Facets on these asymptotically flat interfaces may strongly influence their mechanical response for several reasons. First, the presence of the low-energy facets at an interface reduces the interface energy and increases mechanical and thermal stability. For instance, Cu-Nb interfaces with terraces, fabricated by the accumulative roll bonding (ARB) technique [1], possess great thermal stability and can persist in despite of severe plastic deformation [2,3]. In addition, the local stress state near facets at an interface is generally distinct from the applied stress state, e.g., a remote, pure normal or shear loading to the originally flat interface would be transformed to a local, combined normal/shear loading on the facets [4,5]. Such a change in stress state has been demonstrated to tailor segregation of rare earth elements along the twin boundaries [5–8]. Further, due to the elastic mismatch between the adjoining crystals, stress concentrations tend to be induced at the apices — or ridges and valleys — formed by neighboring facets. These stress concentrations may assist the emission of lattice or

interfacial dislocations, which can be beneficial for interfaces that would otherwise be brittle, e.g. metal/ceramic interfaces [9].

The mechanical response of faceted interfaces may greatly depend on the structures and specific properties of these low energy facets. Coherent facets may possess strong resistance to the nucleation and emission of dislocations as well as slip transmission for dislocations. Semi-coherent facets, similar to semi-coherent interfaces, may facilitate the nucleation of lattice dislocations from the misfit dislocation networks (MDN) [10] in response to normal loading and may slide accompanied with the formation of interlayer dislocation loops at the MDN or by the collective translation of the MDN [11,12]. It is worth noting that the concept of surface/interface facets may be multiscale, varying from the atomic-scale interfacial disconnections/steps to the macroscopic surface facets of single crystals visible to the naked eye. For terraced interfaces, the change in the facet size may alter the coherency and dislocation structure at interface, resulting in different mechanical responses.

Modeling efforts, in pursuit of predicting the morphology of the terraced interfaces/surfaces, mostly follow Herring's initial thermodynamics argument. According to Herring [13], the morphology of the terraced interfaces/surfaces is the result of minimization of interface free energy, which may depend on both orientation and curvature (facet edge energy). While this framework may be effective in predicting the energy and morphology of solid-liquid interfaces, and the like (such as solid-gas interfaces), where the

\* Corresponding author.

E-mail address: [sshao@lsu.edu](mailto:sshao@lsu.edu) (S. Shao).

specific energy of the low-energy facet is only dependent on its orientation [14], its direct application to solid-solid interface should be used with caution. It is evident that the total area of an asymptotically flat interface, when the orientations of facets have been prescribed, is independent of the absolute size of the facets. Yet the facet size has been shown to be quite constant at a given temperature [15]. The governing factors for the facets' characteristic dimensions has been attributed to the minimization of the excess energies associated with the facet junctions (edge energy) [16]. In addition to the minimization of the total edge energy, the key could also lie in the fact that the specific interface energy is a function of not only its orientation, but also a facet's size. To date, mathematical models capable of accurately predicting the morphology of the solid/solid interfaces have been constructed [17]. However, these mathematical models utilized a description of the specific interface energy that is only a function of adjoining crystals' orientation and the interface's habit plane. Because of this, an intrinsic property of the interfacial facets, i.e. their size dependence, cannot be fully captured.

On a terraced interface, depending on the associated lattice mismatch, misorientation of closed-packed atomic planes, and their size, facets may contain characters of dislocations, steps, and disclinations [18–20]. In this work, facets are treated, in a general sense, as super interfacial disconnections (referred to as SIDs) [18,19]. The nomenclature "super" is used here to distinguish the facets from the disconnections in the conventional sense (whose height is on the order of one atomic spacing) [18,19]. A general interfacial disconnection, shown in Fig. 1, is characterized by a Burgers vector,  $\mathbf{b}$ , and a step vector,  $\mathbf{l}$ , which are defined as:

$$\mathbf{b} = \mathbf{l}_\alpha + \mathbf{l}_\beta \quad (1a)$$

$$\mathbf{l} = -l_\beta \quad (1b)$$

where the right-hand, finish-start rule is obeyed [18,19]. Under this setup, a facet/SID is said to contain dislocation and step characters if  $\mathbf{b}$  is parallel/antiparallel to  $\mathbf{l}$ . A facet/SID contains a disclination character if  $\mathbf{b}$  is non-parallel to  $\mathbf{l}$ . Lastly, a facet/SID with a pure step character would require that  $|\mathbf{b}|=0$ .

The energy of a given SID is related to all of its characters: the Burgers vector contributes to its overall coherency strain energy and the step vector contributes to its overall surface energy. To the first order of approximation, the total energy of a SID, per unit length in  $\xi$  direction, can be expressed as

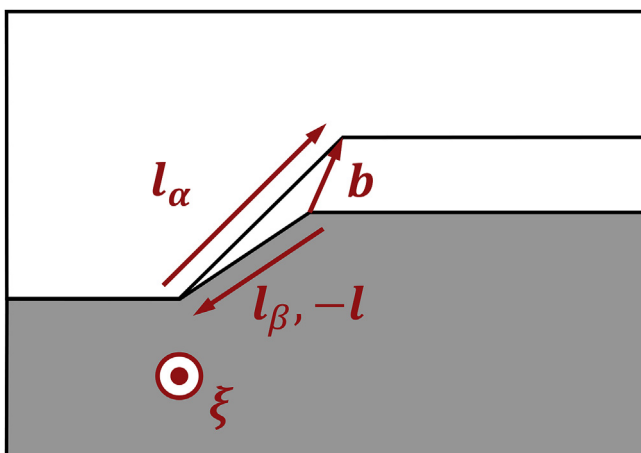


**Fig. 1.** A schematic illustration of an interfacial disconnection.

$$\frac{E_{disc}}{L} = \frac{E_b}{L} + \frac{E_l}{L} \quad (2a)$$

$$\frac{E_b}{L} = \frac{k\alpha\bar{\mu}|\mathbf{b}|^2}{4\pi} \ln \frac{R}{r} \quad (2b)$$

$$\frac{E_l}{L} = \gamma(\mathbf{l})|\mathbf{l}| \quad (2c)$$

Here  $k$  is a factor accounting for the differences in the strain energy between a dislocation and a disconnection,  $\alpha$  accounts for the character of a disconnection, i.e.  $\alpha = 1$  for screw and  $\alpha = 1/(1-\nu)$  for edge,  $\bar{\mu}$  is an effective shear modulus at interface. Note that Eqn. (2b), with the form of the line energy of an edge dislocation, is merely an approximation as the core energy part of the disconnection obviously differ from that of a regular dislocation. In addition, isotropic assumption is used here, while crystals are anisotropic in general in reality. Due to the mismatch in elastic properties, the strain field of interfacial dislocations/disconnections differs from that of ones in bulk [21]. By using the parameter  $\bar{\mu}$ , the effect of the heterophase interfaces on the strain energy of these line defects can be approximated [22]. With the change in size  $|\mathbf{l}|$ , the energy of a disconnection,  $\frac{E_{disc}}{L}$ , changes, as both the Burgers vector and the surface energy  $\gamma(\mathbf{l})$  may vary. In addition, the specific facet energy per unit area, evaluated as  $\gamma_{facet} = E_{disc}/(L|\mathbf{l}|)$ , may vary, not only as a function of the direction of the step vector ( $\mathbf{l}/|\mathbf{l}|$ ), but also of its magnitude ( $|\mathbf{l}|$ ). It follows that minimization of overall interfacial energy would inevitably involve the minimization of  $\gamma_{facet}$ . However, how this specific facet energy of a disconnection evolves as a function of its size  $|\mathbf{l}|$  has not been clearly elucidated in the literature.

To shed some light on this complexity, this work focuses on a simplified case of facets/SIDs, i.e. ones with only dislocation + step characters. Atomistic simulations performed on faceted Cu-Ni (111) semi-coherent interfaces are utilized to investigate the structural, energetic, and mechanical characteristics of interfacial facets (or SIDs). Semi-coherent interfaces are considered here due to their ubiquitous nature in a wide range of materials [23], including precipitation hardened alloys [24–29], eutectic alloys [30,31] and nano-multilayered composites [32–38]. The contribution of this work is twofold: (1) a mechanism, by which the facet energy,  $\gamma_{facet}$ , (hence the interface energy) varies as a function of SID's size, is elucidated; (2) the role of SID's size on the interfacial mechanical response, to both compression and shear is revealed and analyzed in detail. Although this work is performed on a particular material system, i.e. FCC Cu and FCC Ni, the findings are expected to be applicable to a broader range of semi-coherent interfaces between materials with same lattice structure. This rest of this article is organized as follows: Section 2 details the methodology we have adopted for the atomistic simulations and analyses of the results. In Section 3, we present the main findings of this work, which pertain to the structures (Section 3.1), energy characteristics (Section 3.2), and the mechanical responses (Section 3.3) of interfacial facets. In Section 4, we provide detailed discussion of our results, regarding the limitations of the present work, and the implications of our findings to related fields. Finally, in Section 5, we draw our conclusions.

## 2. Methodology

In this work, we use molecular statics (MS) and molecular dynamics (MD) performed using the parallel atomistic simulation program LAMMPS [39] to investigate the structure, energies, and mechanical responses of the faceted Cu-Ni (111) semi-coherent

interfaces. The interactions among Cu and Ni atoms [40] are modeled by the embedded atom method (EAM) [41,42]. This particular set of potentials can reliably reproduce a broad range of materials properties of Cu, Ni and Cu-Ni compounds, including melting points, enthalpy of mixing, ground state lattice structures, point defect formation energies, etc. The authors are aware of the negative free energy (Gibbs) of mixing of the Cu-Ni system at finite temperatures, which dictates that a thermodynamic driving force exists for Cu to alloy with Ni. This arise from Cu-Ni system's slightly positive mixing enthalpy and the positive mixing entropy ( $G = H - TS$ ). We stress that the interfacial alloying effect is not among the foci of this study. Instead, the focus of this paper is on the diffusionless, displacive characteristics, such as structure of the MDNs, nucleation/emission of dislocations from interface, etc., that are shared by the entire class of the (111) FCC-FCC semi-coherent interfaces. The results of this paper is not expected to be strongly influenced by the Cu-Ni intermixing, as time scale for such a process is much longer as compared to the nanosecond time scale of MD.

For computational simplicity, an asymptotically flat, faceted interface is not modeled, as that would require a computational cell that is too large, due to the imposed periodic boundary conditions. Instead, Cu-Ni bi-crystals containing a pair of disconnections with opposite signs are modeled, as shown in Fig. 2. As shown, the same crystallographic orientation,  $x/[1\bar{1}\bar{2}] z/[1\bar{1}0]$  and  $y/[111]$ , is obeyed by all atomistic models. The interface<sup>1</sup> plane is perpendicular to the  $y$ -direction. Each model has a dimension of  $32.8 \times 18.9$  nm in the  $x$ - $z$  plane. Under zero strains, this box would fit 74 and 76 periodic lengths of Cu and Ni in the  $x$  and  $z$  directions, respectively, which corresponds to 26.751 and 26.752 nm. Due to the applied boundary conditions, these dimensions yield strains in the Cu and Ni layers below  $5 \times 10^{-5}$ , which correspond to  $\sim 10$  MPa of stress. Note that the smallest  $x$ - $z$  dimension to satisfy this condition is  $16.4 \times 9.5$  nm [10], the in-plane dimensions in the present study are enlarged by a factor of four to increase the probability of observing dislocation nucleation events. Periodic boundary conditions are applied in the  $x$  and  $z$  directions, while fixed boundary conditions are applied in  $y$  direction. As shown in Fig. 2, regions on top and bottom of the models, with thickness of 10 Å, are fixed, as denoted by the brown-colored atoms. Obeying the periodic boundary conditions, in each model, two disconnections are created on the interface, along the close packed (111) plane. To investigate the effect of the disconnection height ( $h$ )—or length of step vector ( $|l|$ ), a total of more than 24 atomistic models have been created, corresponding to  $h = 0\text{--}20$  nm or  $|l| = 0\text{--}21.3$  nm. To minimize boundary effects, a minimum distance of  $d = 10$  nm between the interface and the fix boundaries is guaranteed in all models.

Following the methods used by prior works [10,12,43,44], the residual stresses of initial structures was iteratively relaxed. The resulting structures has a state of stress  $\sigma_{yy}^{Cu}, \sigma_{yy}^{Ni} \approx 0$  and  $\sigma_{xx}^{Cu}, \sigma_{zz}^{Cu}, \sigma_{xx}^{Ni}, \sigma_{zz}^{Ni} < 10$  MPa. This stress relaxation is necessary, as the calculation of interfacial energies could be significantly affected by the residual coherency strains [24]. Followed by relaxation, each structure is mechanically loaded under three stress-controlled shear and compression conditions. The applied shear stress is parallel to the interface and along  $x$  directions ( $\sigma_{xy}$ ), the applied compression is perpendicular to the interface ( $\sigma_{yy}$ ). The choice of these loading conditions was dictated by the following reasons: (1) the introduction of parallel disconnections has been shown to strongly strengthen an interface's shear resistance along the perpendicular direction [45], namely  $x$  direction in the present

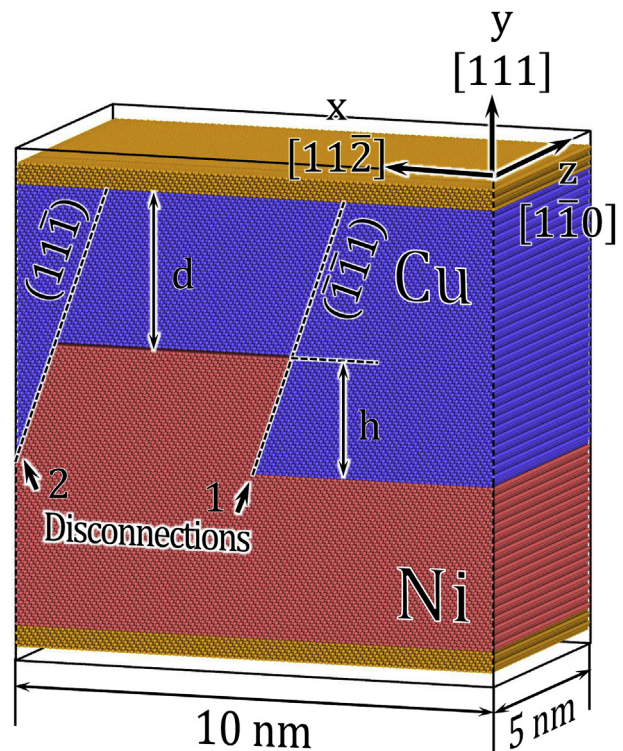


**Fig. 2.** Illustration of atomistic configurations of the interfacial models containing disconnections. Blue atoms are Cu, red atoms are Ni, while brown atoms are fixed during the MS/MD simulations. (For interpretation of the references to color in this figure legend, the reader is referred to the Web version of this article.)

study; (2) typical loading conditions in the experiments, pillar compression [46–48] and nanoindentation [49,50], etc., typically involves compression and/or shear loading on the interfaces. Indeed, simulations of shear loading along  $z$  direction ( $\sigma_{yz}$ ) of the terraced interfaces performed in this work revealed little strengthening effect (strengths about 200 MPa). The loadings were iterative and 50 MPa was applied at each loading step. At each loading step, the following boundary conditions are ensured:

$$\begin{aligned} \text{(for shear)} \quad \sigma_{xy}^{Cu} &= \sigma_{xy}^{Ni}, \\ \frac{1}{2} (\sigma_{xx}^{Cu} + \sigma_{xx}^{Ni}) &= 0 \\ \frac{1}{2} (\sigma_{zz}^{Cu} + \sigma_{zz}^{Ni}) &= 0, \\ \sigma_{yy}^{Cu} = \sigma_{yy}^{Ni} &= 0 \end{aligned} \quad (3a)$$

$$\begin{aligned} \text{(for compression)} \quad \sigma_{yy}^{Cu} &= \sigma_{yy}^{Ni}, \\ \frac{1}{2} (\sigma_{xx}^{Cu} + \sigma_{xx}^{Ni}) &= 0 \\ \frac{1}{2} (\sigma_{zz}^{Cu} + \sigma_{zz}^{Ni}) &= 0, \end{aligned} \quad (3b)$$

Detailed explanations on the application of the stress controlled shear loading has been given elsewhere [12,46] and will not be reiterated here. During loading the temperature is maintained at 5 K.

The evaluation of  $\gamma_{\text{facet}}$  as a function of  $|l|$  is achieved by measuring the interface energy in two ways, namely the projected interface energy ( $\gamma_{\text{Proj.}}$ ) and the specific interface energy ( $\gamma_{\text{Spec.}}$ ), see Eqn. (4). Isolated measurement of  $\gamma_{\text{facet}}$  for a single facet is not

<sup>1</sup> Here, the “interface” refers to the regions of the interface excluding the disconnections.

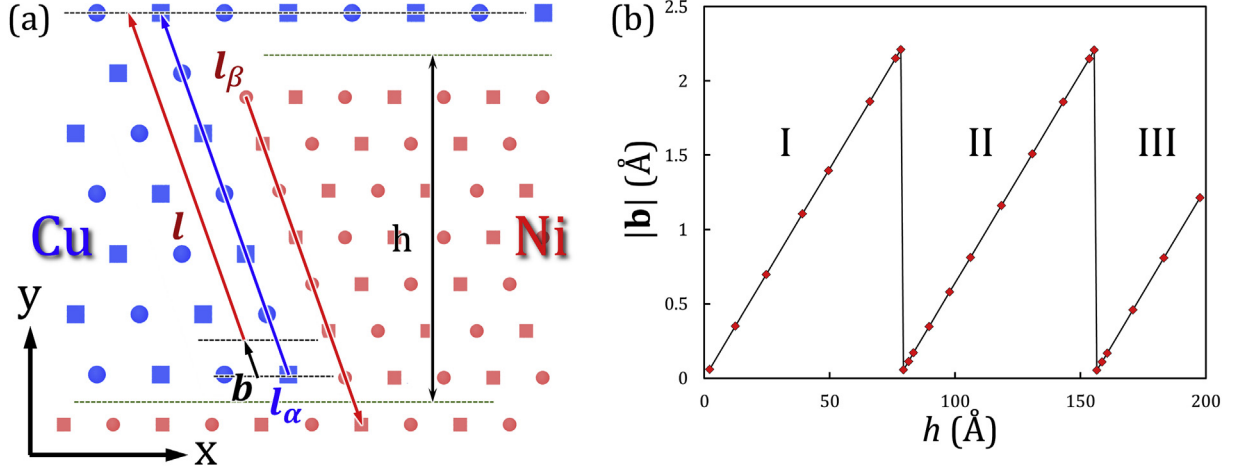


**Fig. 3.** (a) Schematic illustration of the relation between  $\mathbf{l}$ ,  $\mathbf{l}_\alpha$ ,  $\mathbf{l}_\beta$  and  $h$  in the context of Disconnection 1 on a FCC (111) semi-coherent interface. Blue symbols denote Cu atoms, red symbols denote Ni atoms. Squares and circles denote the AB stacking of FCC in the <110> direction. Lattice mismatch between Cu and Ni has been exaggerated. Squares and circles denote A-B stacking on the (110) plane of an FCC crystal. (b) Relation between the nominal magnitude of the disconnection Burgers vector ( $|\mathbf{b}|$ ) and disconnection height ( $h$ ). (For interpretation of the references to color in this figure legend, the reader is referred to the Web version of this article.)

feasible as various energy components of the atomistic system are highly coupled. However, the measurement of  $\gamma_{\text{Spec.}}$  is expected to well correlate with  $\gamma_{\text{facet}}$ . The aforementioned qualities are evaluated according to the equations below:

$$\gamma_{\text{Proj.}} = \frac{1}{A_{\text{Proj.}}} (E_{\text{Interface}}(N_{\text{Cu}}, N_{\text{Ni}}) - N_{\text{Cu}}E_{\text{Cu}} - N_{\text{Ni}}E_{\text{Ni}}) \quad (4a)$$

$$\gamma_{\text{Spec.}} = \frac{1}{A_{\text{total}}} (E_{\text{Interface}}(N_{\text{Cu}}, N_{\text{Ni}}) - N_{\text{Cu}}E_{\text{Cu}} - N_{\text{Ni}}E_{\text{Ni}}) \quad (4b)$$

where  $N_{\text{Cu}}$  and  $N_{\text{Ni}}$  are the respective number of atoms for Cu and Ni in a bicrystal atomistic model,  $E_{\text{Interface}}$  is the total energy of the bicrystal model,  $E_{\text{Cu}}$  and  $E_{\text{Ni}}$  are the respective per atom energies for Cu and Ni under bulk condition,  $A_{\text{Proj.}}$  is the area of an interface projected to the x-z plane (calculated as the x-z cross-section area of the bicrystal model),  $A_{\text{total}}$  is the total area of an interface accounting for the area of the facets. The  $A_{\text{total}}$  total area for a terraced interface (with step height  $h$ ) is calculated according to the total number atoms immediately adjacent to the interface  $N_{\text{int}}^{h \neq 0}$ . The area ( $A_{\text{flat}}$ ) and the number of interfacial atoms ( $N_{\text{int}}^{h=0}$ ) of the flat (111) interface are used as references. The area of any terraced interface can then be calculated as  $A_{\text{total}} = \frac{N_{\text{int}}^{h \neq 0}}{N_{\text{int}}^{h=0}} A_{\text{flat}}$ .

### 3. Results

#### 3.1. Structure of FCC (111) semi-coherent interfaces and disconnections

The disconnections on the Cu-Ni (111) semi-coherent interface exist on the (11̄1) and (11̄1̄) planes of both crystals, assuming that the plane normal points from Ni to Cu. The step vector of the respective crystals,  $\mathbf{l}_\alpha$  and  $\mathbf{l}_\beta$ , are antiparallel. This is schematically shown in Fig. 3a, using the Disconnection 1 as an example. In addition, due to the bulk lattice mismatch between Cu and Ni of around 2.7% the character of the disconnections on this type of interfaces is not always pure step. The corners of this disconnection are formed by {111} interfacial facets with a 70.5° angle. It is trivial to show that the opposing disconnection to the one shown in Fig. 3a has an opposite Burgers vector. The pair of disconnections,

i.e. disconnections 1 and 2 in Fig. 2, therefore exists as a dipole. In addition, the Burgers vector of these disconnections varies as a function of the disconnection height  $h$ , or step vector length  $|\mathbf{l}|$ . Indeed, as shown in Fig. 3b, the  $|\mathbf{b}|$  appears to be periodic function of  $h$ , whose period is ~77 Å. This behavior can be rationalized by observing that the spacing between the {111} planes in Cu and Ni is  $d_{\{111\}}^{\text{Cu}} = 2.087$  Å and  $d_{\{111\}}^{\text{Ni}} = 2.032$  Å, respectively, and that at  $h = 77.2$  Å the Cu and Ni terraces on either side of the disconnection are almost of equal height—with a mismatch of only 0.004%. This suggests that the Burgers vector of a disconnection on the Cu-Ni (111) interface is 0 when  $h = n \mathcal{H}$ , where  $n$  is an integer, and increase piece-wise linearly with the disconnection height. When  $h$  is just below  $n \mathcal{H}$ , the addition of one extra atomic plane creates misfit dislocations on the facet of the disconnections.<sup>2</sup>

Depending on the height of the interfacial disconnections, the dislocation structure on the facet of disconnections may display distinct features. Fig. 3 shows three typical structures of disconnections, corresponding to Cases I, II and III noted in Fig. 3b. Detailed disregistry analyses, examples of which shown in the Suppl. Mater. Section S2, have been performed, revealing the characteristics of the dislocations. As shown in the atomistic configurations, the misfit dislocations displayed a very noticeable spiral pattern at nodes. This phenomenon has been reported explained in detail by Shao et al. [10,43]. For Case I, the facet of the disconnection is coherent along the step vector  $\mathbf{l}$  (recall Fig. 3a). In this case, if using the step vector as a search vector,<sup>3</sup> the net Burgers vector content (from MDN, which is different from the  $\mathbf{b}$  defined in Eqn. (1a)) is 0 over the distance encompassed by the disconnection. Indeed, as shown in Fig. 4a, the facet of the disconnection only contains dislocations with line sense near-parallel to the  $\gamma\bar{D}$  direction with no intersection with the search vector. The net Burgers vector along the z direction over the entire dimension of the computational cell is  $B_z = 2(B_y + \gamma A) = 2BA = \bar{a}[1\bar{1}0]$ , where  $\bar{a}$  is the lattice constant of a interfacial reference lattice, on which the Burgers vectors of interfacial dislocations are formally defined [20].

<sup>2</sup> In passing, “facet of disconnections” will exclusively refer to facets on the (11̄1) and (11̄1̄) planes; while “facet of the interface” will exclusive refer to facets on the (111) plane in this article.

<sup>3</sup> The concept of “search vector” was first proposed by Frank [73] and Bilby [74]. Later on, this has been widely used by a number of researchers in their follow up work [20,75,76].

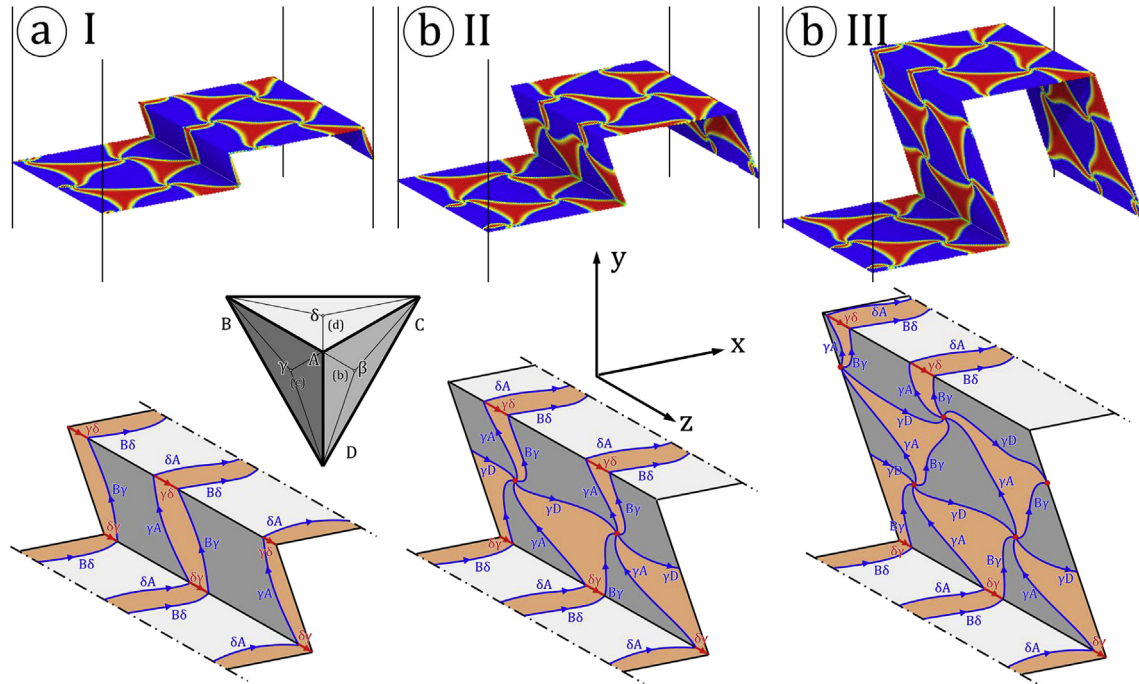


**Fig. 4.** Structures of the disconnections for Cases I, II and III noted in Fig. 3(b) have been shown in (a), (b) and (c), respectively. Top half of the figures shows the atoms on the interfaces colored by centro symmetry parameter (CSP), where red correspond to CSP = 6 and blue correspond to CSP = 0. Bottom half of the figures schematically shows the corresponding dislocations structures. Burgers vectors of the dislocations are given following the Thompson's convention, the Thompson's tetrahedron (TT) is also shown as an inset. The TT is oriented so that  $x/\delta C$ ,  $y/D\delta$  and  $z/BA$ . (For interpretation of the references to color in this figure legend, the reader is referred to the Web version of this article.)

For Case II, the facet of the disconnection is semi-coherent along the step vector **I**. Treating the positive  $z$  direction as the line sense of the disconnection, the net Burgers vector along the search vector, as shown in the [Section S1 of the Suppl. Mater.](#), varies depending on the position of the search vector on the  $z$  axis. However, with the occurrence of a horizontal dislocation  $\gamma D$  and inclined dislocations  $\gamma A$  and  $B\gamma$ , the average net Burgers vector is  $1.5\gamma D$ . When projected to the  $y$  direction,  $1.5\gamma D$  equals  $\delta D$ , which is identical in magnitude with the (111) planar spacing at the disconnection. At the step height of  $h = \mathcal{H}$ , the step vectors for both Cu and Ni are equal and opposite, i.e.  $\mathbf{l}_x = -\mathbf{l}_y$ . From Fig. 3, it is apparent that the largest possible Burgers vector of the disconnection in Case I is  $1.5\gamma D$  (observe that the largest gap formed on the terrace between Cu and Ni is one (111) planar spacing). In this case, the zero Burgers vector of the disconnection can be regarded as the result of the cancellation due to the sudden onset of the net Burgers vector of the MDN along the step vector **I** on the facet of the disconnection. In Case II, the net Burgers vector along  $z$  direction has not been altered and is identical to Case I, i.e.  $B_z = 2(B\gamma + \gamma A) = 2BA$ . Also similar to Case I, the maximum Burgers vector of the disconnection achievable for Case II is  $1.5\gamma D$ . Further increase in the disconnection height induces the onset of Case III.

For Case III, an additional horizontal dislocation  $\gamma D$  appears on the facet of the disconnection. The net Burgers vector of the MDN along the step vector is invariantly  $3\gamma D$  on this facet, regardless of the location of the search vector on the  $z$ -axis. Similar to the prior case, the Burgers vector of this disconnection is zero at the onset of this regime, and grows to a maximum of  $1.5\gamma D$  with the increasing step vector (correspondingly, the increasing step height).

The illustrated disconnection in Fig. 4 exist on the (c) plane of the Thompson's Tetrahedron (TT) [51,52]—corresponding to the (111) plane in Miller indices. The complex dislocation structure on the facet of the disconnection continues on to the (d) plane ((111) plane in Miller indices). The stacking faults of the connecting

planes, shown as brown-colored regions in the bottom panels of Fig. 4, join by stair-rod dislocations with Burgers vector of  $\gamma\delta$ . These stair-rod dislocations exist between stacking faults at the corners of the disconnection, forming an acute angle of  $70.5^\circ$ . Analyses so far has centered on the structure of one disconnection in the disconnection conjugate on the (111) interface plane whose facet's plane normal facing Cu side is along  $C\gamma$ . Structure of the second disconnection (Fig. 5) in the disconnection pair, whose plane normal facing Cu side is along  $\gamma C$ , are quite similar to the first one. A noticeable difference is that the stair-rod dislocations (with greek-greek type Burgers vectors) now exist between stacking faults forming an obtuse angle of  $109.5^\circ$ . Detailed structure of the stair-rod dislocation at location 1 in Fig. 5a, has been provided in Fig. 5b. This stair-rod dislocation has a Burgers vector of  $\gamma\delta/BA$  following the convention by Thompson [51]. All of stair-rod dislocations observed so far “turns” stacking faults from one slip plane to another. Another family of these turns (such as one at location 2 in Fig. 5a) is of the contracted type, as illustrated by Fig. 5c. The morphology of the intersection is dominated by the attraction/repulsion force between partial dislocations on the same and opposite sides across the obtuse intersection line, which has been discussed in detail by Hirth and Lothe [52].

### 3.2. Energy of FCC (111) semi-coherent interfaces with disconnections

Energy of disconnections are functions of both their step vector and Burgers vector. Therefore, the interface energy —per unit area— is expected to vary as a function of these parameters. In addition, since the Burgers vector of a disconnection has been shown, in the previous section, to be a function of the step vector, the interface energy of the faceted (111) interface may experience certain periodic features as the height of the disconnections is gradually increased. Fig. 6a shows the variation in the projected

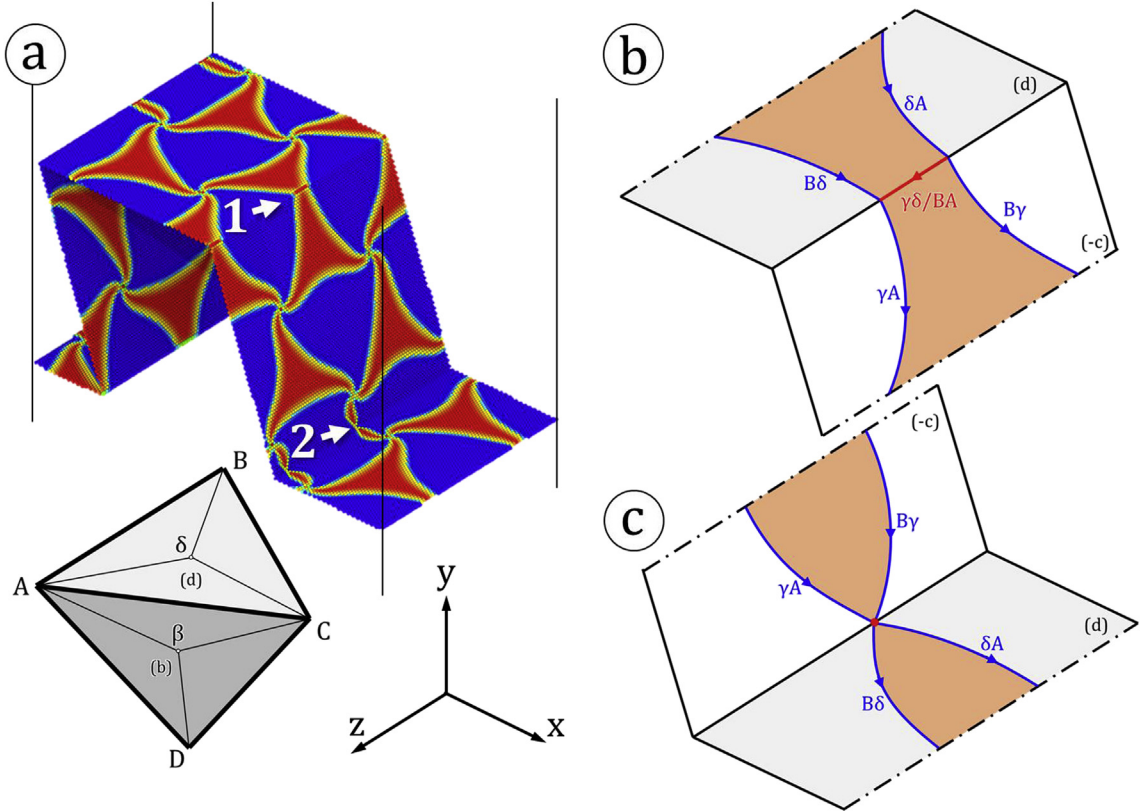


**Fig. 5.** Special types of dislocation junctions that “bend” dislocation and stacking faults from one plane to another, existing on the facet plane that forms an obtuse angle with the interface plane (a). This facet plane has been marked as (-c) plane to denote the viewing direction from inside of the TT (not visible). (b–c) show the detailed structures of these special-case junctions, marked by numbers 1 and 2, respectively.

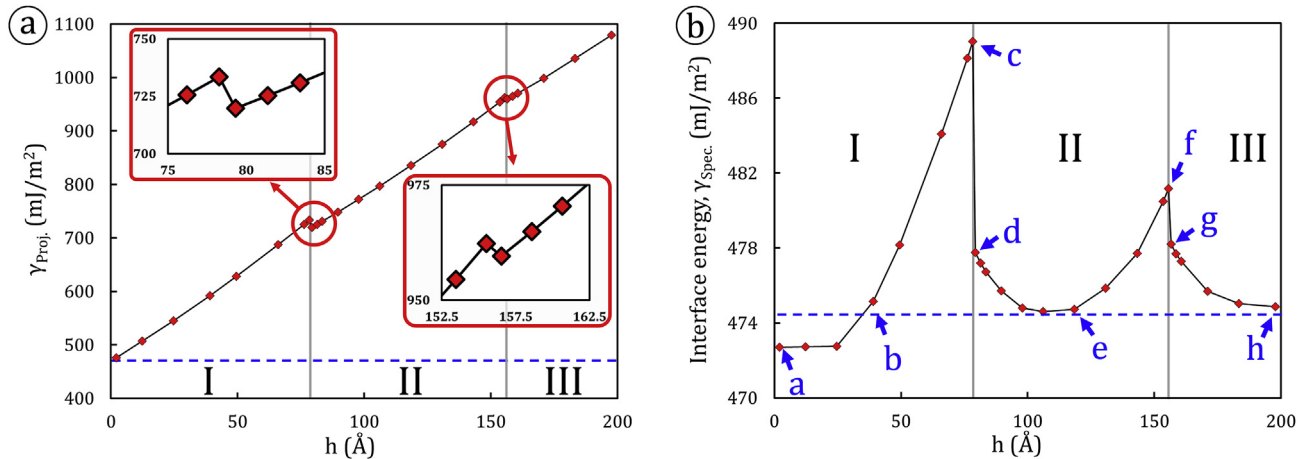


**Fig. 6.** Calculated interface energy, per unit area, based on two accounts: (a) excess energy of an interface divided by the projected interface area on the x-z plane, denoted as  $\gamma_{\text{Proj}}$ , (b) excess energy of an interface divided by the total interface area, including the area of the facets, denoted as  $\gamma_{\text{Spec}}$ . The blue horizontal dashed lines denote the case of the flat interface. (For interpretation of the references to color in this figure legend, the reader is referred to the Web version of this article.)

interfacial energy,  $\gamma_{\text{Proj}}$ , as a function of the disconnection height  $h$ . It is evident that this energy increases approximately linearly with increasing  $h$ . This indicates that the step component (Eqn. (2c)) dominates the energy of a disconnection. Indeed, the interface energy of a flat, semi-coherent (111) Cu-Ni interface is around 470 mJ/m<sup>2</sup>, the introduction of a pair of disconnections with facet area comparable to that of the facets of interface is expected to substantially increase the interface energy. It is also worth noting that near the boundaries between cases, drops of interface energy

exist, as shown in the insets of Fig. 6a. This indicates the influence of disconnection's Burgers vector on interface energy, although small as compared to that of the step vector. A baseline reference, i.e. the interface energy of the flat Cu-Ni (111) interface (~475 mJ/m<sup>2</sup>), is given in Fig. 6 as blue dashed lines. Note that this energy is close to, but lower than, the  $\gamma_{\text{Proj}}$  for  $h = 2$  Å.

To isolate the effect of disconnections' Burgers vector, specific interface energies ( $\gamma_{\text{Spec}}$ , Eqn. (4b)) are calculated, which account for the area of the disconnections' facets in the total interfacial area.

As shown in Fig. 6b, the specific interfacial energy fluctuates in the range of  $470 \text{ mJ/m}^2 \sim 490 \text{ mJ/m}^2$ . The variation in  $\gamma_{\text{Spec}}$  shows qualitative correspondence with the nominal variation in Burgers vector as the height of disconnections gradually increases. Obvious drops of specific interface energy occur at the boundaries between Cases I, II and III, although it is interesting to note that within the domain of each case (Fig. 6b), the specific interface energy does not monotonically increase as the increase of the disconnection height within each case. Instead, small drops in specific interface energy exist before its eventual increase.

This phenomenon indicates that, even though the strain energy associated with a disconnection (first term on the right hand side of Eqn. (2a)) may increase as the magnitude of its Burgers vector increases, the facet energy— $\gamma(\mathbf{l})$ , a per unit area quantity—may decrease. Indeed,  $\gamma(\mathbf{l})$  includes the contributions from both the core energies of the MDN and the energies of the coherent regions, both of which are influenced by the applied stress on the interface plane [24]. As was shown by Shao et al. [24], the flat interface energy may increase as much as  $50 \text{ mJ/m}^2$ , when a tensile stress of  $8 \text{ GPa}$  is applied normal to the interface. Indeed, a fully coherent Cu-Ni interface, depending on its orientation, may incur a coherency stress of several GPa [53]. As the Burgers vector of the dipolar disconnections increases, stresses in the regions between the disconnections increases noticeably due to their coupling. This can be observed in Fig. 7(a-h), which shows the distribution of volumetric strain in both Cu and Ni on the x-y plane. Each letter designation of these sub-figures corresponds to a lettered data point in Fig. 6. It can also be readily shown that other components of strains behave in a similar manner. These varying strain fields as a function of the disconnection's Burgers vector modifies the energies of the {111} facets.

The impact of Burgers vector on the elastic strain energy of the disconnections can also be quantified. Fig. 7(r-y) shows the distributions of average per atom excess potential energy on the x-y planes for models corresponding to the lettered data points in Fig. 6b (r-y in Fig. 7 correspond to points a-h in Fig. 6b). It is evident that the atoms on the interfacial facets exhibits potential energies that severely deviate from the respective cohesive energies of pure Cu and Ni under bulk conditions. This is due to the strong influence of the chemical interaction energy between Cu and Ni and the core energy of the MDN. To the first order of approximation, the strain energy of a bicrystal due to the disconnections can be quantified by integrating the per atom excess potential energy over the volume excluding interfacial regions. For convenience, the interface region is numerically defined as an ensemble of atoms near/at the interface plane that possess an excess potential energy of  $|E_{\text{Ex},i}| > 0.0006 \text{ eV}$ , where  $i$  stands for the species of the atom. The total excess energy per bicrystal model divided by the length of the model in z direction would yield an energy per unit length,  $\frac{E_{\text{Tot}}}{L}$ , which correlates with the strain energy per unit length of disconnection,  $\frac{E_{\text{disc}}}{L}$ .

For convenience, the former quantity,  $\frac{E_{\text{Tot}}}{L}$ , for each atomistic model has been normalized by the line energy of a screw type Shockley partial ( $E_{\text{SP}}$ ) in a hypothetical FCC crystal and presented in Fig. 8a. The hypothetical crystal has a lattice constant and elastic moduli identical to the average between those of Cu and Ni, such that  $\bar{a} = 3.57 \text{ \AA}$  and  $\bar{\mu} = 62 \text{ GPa}$ . The lower and upper bounds of integration have been chosen as  $r = 1 \text{ nm}$  and  $R = 16 \text{ nm}$ , the latter corresponds to the spacing of the disconnections in the present work. Lettered data points correspond to those identified in Fig. 6b. It is noted from Fig. 8a that the energy minima do not reside at zero level. This is likely due to the non-vanishing stress-field near a semi-coherent interface. The total defect strain energy per unit length,  $\frac{E_{\text{Tot}}}{L}$ , can also be plotted against the nominal magnitude of

disconnections' Burgers vector (Fig. 8b). Treating this non-vanishing energy as a constant ( $\frac{E_0}{L}$ ), the  $\frac{E_{\text{Tot}}}{L}$  vs.  $|\mathbf{b}|$  curves in Case I to III can be fitted to quadratic functions of the form

$$\frac{E_{\text{Tot}}}{L} = \frac{E_0}{L} + 2km\bar{\mu}|\mathbf{b}|^2 + \mathcal{O}(E_{\text{disc.}}^2) \quad (5)$$

where  $m$ , with a typical form of  $\frac{\ln R/r}{4\pi}$  or  $\frac{\ln R/r}{4\pi(1-\nu)}$ , is a constant that accounts for the character and cylindrical integration boundaries of the disconnection, the second term is essentially identical to Eqn. (2b).  $\mathcal{O}(E_{\text{disc.}}^2)$  stands for the interaction energy of between the disconnections, which is neglected to the first order of approximation. The quadratic fits are also shown in Fig. 8b. The fit parameters, normalized by  $\frac{E_{\text{SP}}}{L}$  have been provided in Table 1. The fit returns a factor  $2km\bar{\mu}/\frac{E_{\text{SP}}}{L} \approx 0.8$ , which leads to a  $E_{\text{disc.}}/E_{\text{SP}} = 0.9$  at  $|\mathbf{b}| = 1.46 \text{ \AA}$  (magnitude of the Burgers vector of a Shockley partial in the aforementioned hypothetical crystal). This indicates that the  $k$  factor in Eqns. (2b) and (5) has a near-identity value.

### 3.3. Mechanical response of FCC (111) semi-coherent interfaces with disconnections

Two different types of loading conditions, i.e. normal-to-interface compression ( $-\sigma_{yy}$ ) and parallel-to-interface shear ( $\sigma_{yx} > 0$  or  $\sigma_{yx} < 0$ ), were applied to the bicrystal models to investigate the interfaces' response, in terms of both strength and unit deformation mechanisms. Under both loading conditions, the interfaces always first emit dislocations into the Cu layer. This is ascribed to the lower energy barrier associated with the nucleation/emission process, which is due to the lower elastic constants—therefore lower dislocation line energy—and the lower stacking fault energy in Cu. In addition, the dislocations almost always (aside from a few models with very small disconnection heights) emit from the edges of the disconnections. Depending on the loading condition, loading direction, and the dislocation structure of the disconnections, the mechanisms via which the dislocations nucleate and emit vary. In addition, correspondence between the disconnection's structure, Burgers vector and interfacial strength exist.

#### 3.3.1. Dislocation nucleation/emission from interface under compression

Under compressive loading ( $-\sigma_{yy}$ ), the interfaces containing Case I disconnections may nucleate/emit dislocations via two mechanisms depending on the disconnection height ( $h$ ). For smaller disconnection heights, i.e.  $h < 25 \text{ \AA}$ , the dislocations nucleate from the condensed dislocation nodes on the horizontal portions of the interface. This mechanism is same as that at flat interface, which has been documented previously [54].

At  $h > 25 \text{ \AA}$ , another mechanism is activated (Fig. 9). The step-by-step process is shown in Fig. 9a-e, which is viewing the (c) plane along the vector  $\mathbf{v}/|C\gamma||/[111]$ . Detailed disregistry analyses have been performed (shown in the Suppl. Mater. Section S3) to characterize the dislocation structures during the process, which are shown in Fig. 9f-j, which correspond to the sequence shown in Fig. 9a-e. The blue lines with directions in this figure and the following figures denote the Shockley partial dislocation lines; red segments are the stair-rod dislocations identified in Figs. 4 and 5; while blue segments denote the complex dislocation junctions formed at the edges of disconnections during the deformation processes. The compression along z-direction, has a resolved shear stress (RSS) along the slip systems (c)- $\gamma A$  and (c)- $B\gamma$ , with a Schmidt factor of 0.157. Under this RSS, dislocations  $\gamma A$  and  $B\gamma$  bow out and extend the width of the stacking faults (green arrows in Fig. 9h).

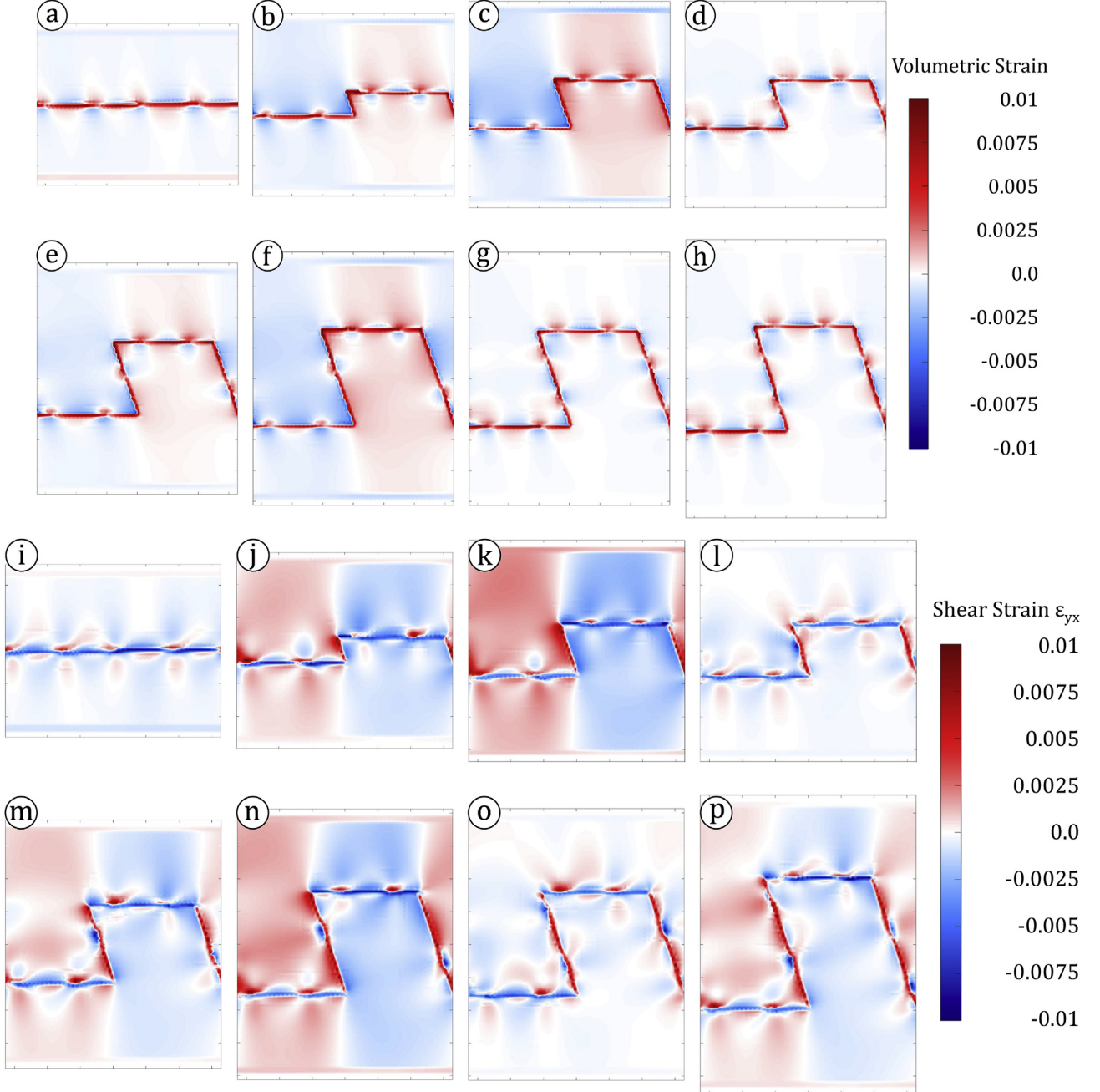


**Fig. 7.** (a–h) Distribution of volumetric strain in the bicrystal models in the x-y plane. Each data point represents the average value along the z direction. The subfigures, respectively, correspond to points a – h in Fig. 6b. (i–p) Distribution of shear strain in the bicrystal models in the x-y plane. Each data point represents the average value along the z direction. The subfigures, respectively, correspond to points a – h in Fig. 6b. (r–y) Distribution of per atom excess potential energy near interfaces, on the x-y plane, corresponding to the data points marked in Fig. 6b. Each data point corresponds to an average value along the z-direction. The subfigures, respectively, correspond to points a – h in Fig. 6b. The reference cohesive energies for Cu and Ni are 3.54 eV and 4.45 eV, respectively, according to Onat and Durukanoglu [40].

Continued bowing extends the dislocation half loops beyond the interface and into the Cu crystal. At the location of one stair-rod dislocation, a dislocation loop  $D\gamma$  nucleates inside of an existing stacking fault region (Fig. 9g). Immediately after its nucleation, dislocation loop  $D\gamma$  expands, which is followed by the extension of the stair-rod dislocation associated with the creation of two partials  $B\gamma$  and  $\gamma A$  (Fig. 9h). A six-fold dislocation node (red dot in Fig. 9i) has therefore been formed, which is identical to dislocation nodes on a generalized FCC (111) semicoherent interface, barring differences in the characters of the surrounding dislocations due to their

directions. Nucleation of small dislocation loops near dislocation junctions and the their subsequent growth has been well documented [10,12], and were ascribed to the relieve of the concentrated core energies. Subsequently, the partials  $\gamma A$  with opposite lines directions annihilate (green, double headed arrow in Fig. 9h), a more complex dislocation junction structure therefore forms (green line segment in Fig. 9i). The approaching loops of  $D\gamma$  and  $\gamma A$  inside Cu can therefore annihilate (Fig. 9i). As a result, a perfect dislocation DA, dissociated into partials  $\gamma A$  and  $D\gamma$  is emitted into the Cu layer. A new type of dislocation pattern, nearly identical to

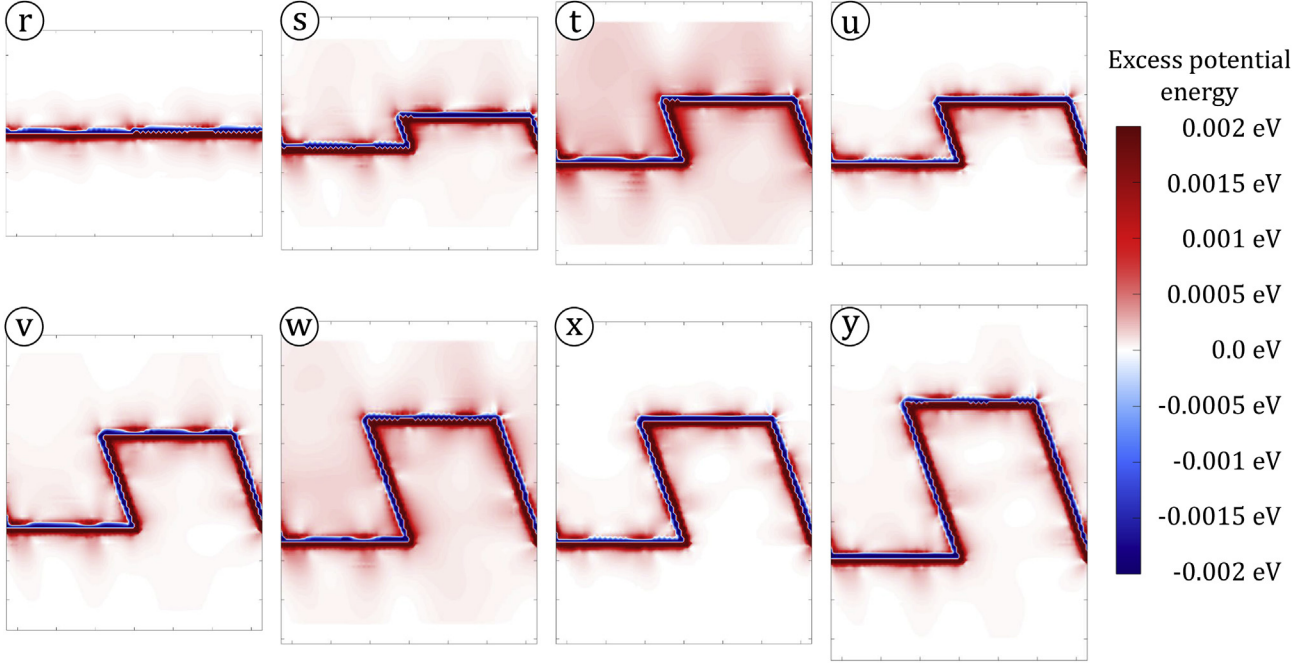


Fig. 7. (continued).

that of the Case II disconnection, is formed in the facet plane.

This operation emits a mixed dislocation (can be both DA or DB) with a strong edge character into Cu. Effectively, this creates an extra (111)<sub>Cu</sub> plane on the positive side of the (c) plane, along  $-v$  direction as shown in Fig. 9. Concomitantly, an extra half (111)<sub>Ni</sub> plane is created on the Ni sited of the facet. Note that this is a strictly mass-conservative operation by dislocation's nucleation and glide, and no diffusion is involved. Continued compressive loading eventually leads to the emission of a dislocation, with opposite line sense to D $\gamma$  and  $\gamma$ A shown in Fig. 9j, into Ni. Note that under this mechanism, only Disconnection 1 is active, as the operation of Disconnection 2 would first emit a dislocation to Ni, due to the crystal symmetry of FCC, which is energetically less favored.

Cases II and III facets respond differently to compressive loading as compared to Case I. A typical process is shown in Fig. 10. The step-by-step snapshots are provided in Fig. 10a–c, which show the atomic plane on which the facet of a disconnection exist. Of interest is the Disconnection 2, as the contained dislocations tend to

migrate towards the Cu side due to the RSS under the applied compressive stress. Plan views in Fig. 10 are along the  $-v$  direction, which views the triangle ABD from inside of the TT, the ABD plane is therefore designated  $(-c)$ . Dislocation structures here have also been characterized by disregistry analyses. As shown in Fig. 10e and f, the emission process involves the combination of dislocation nodes with stair-rod dislocations, dissociation of dislocations from stair rod dislocations, as well as annihilation between dislocation loops. The net result of such a process is exactly the opposite of the process identified in Fig. 9: it increases the coherency along the step vector direction.

### 3.3.2. Dislocation nucleation/emission from interface under shear loading

Depending on the shear loading direction, i.e.  $\sigma_{yx} > 0$  or  $\sigma_{yx} < 0$ , the deformation mechanism exhibited by the interface varies. Similar to the interfaces' mechanical response to compression, under shear, dislocations emit into Cu from the edges of the disconnections. Therefore, under both shear directions, only the top-

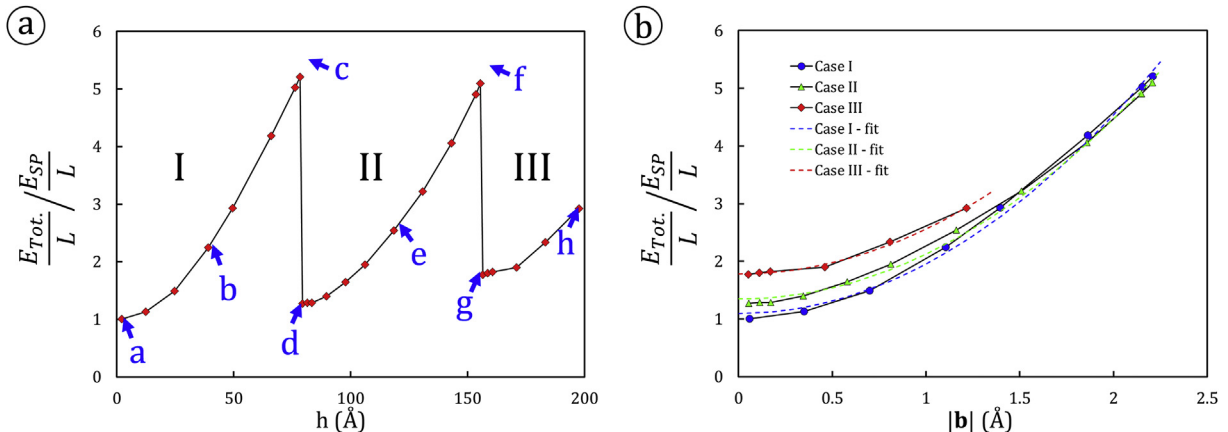


Fig. 8. Normalized total defect energy per unit length as a function of the disconnection height (a) and the magnitude of Burgers vector (b).

**Table 1**

Fit parameters for strain energies associated with terraces formed by a pair of disconnections, per unit length along z direction.

Fit parameters	$2k\alpha\bar{\mu}/Esp$	$Eo/Esp$
Case I	0.86	1.10
Case II	0.78	1.35
Case III	0.78	1.78

most facet of interface is active, as the activation of the bottom facet of interface would emit dislocations into Ni, which is not energetically favored.

When  $\sigma_{yx} > 0$ , the MDN on the facet of the interface migrate towards the  $-x$  direction, which is also the eventual direction along which dislocations are emitted into Cu. The emitted dislocations are Shockley partials of edge type. The process is depicted in Fig. 11. Snapshots of the atomic plane on which the top facet of interface

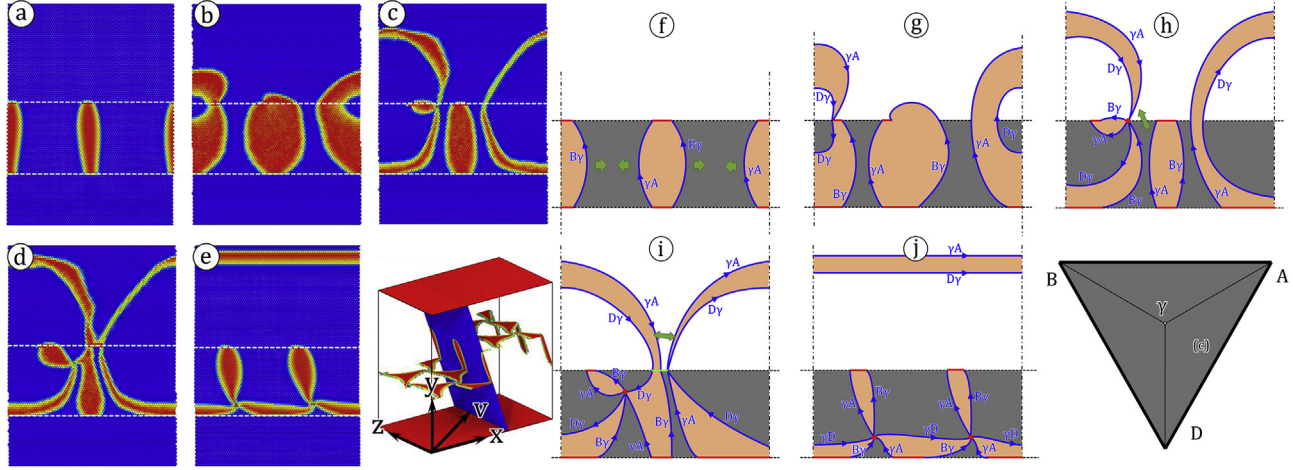


**Fig. 9.** Emission of lattice dislocation from the facets of a Case I disconnection under compressive loading. (a–e): Snapshots of atomic plane aligning with the facet at various stage of the emission process. The relative orientation of this plane with respect to the bilayer model is shown in the accompanying inset. Atoms are colored by the centro-symmetry parameter (CSP), with blue representing CSP = 0 and red representing CSP = 6. (f–j): Dislocation structure characterized by disregistry analyses. Orientation of all two-dimensional representations follows the (c) plane of the Thompson's tetrahedron shown on the bottom right. The dashed lines denote the location of disconnections' edges. The dash-dotted lines denote the location of the periodic boundaries. (For interpretation of the references to color in this figure legend, the reader is referred to the Web version of this article.)

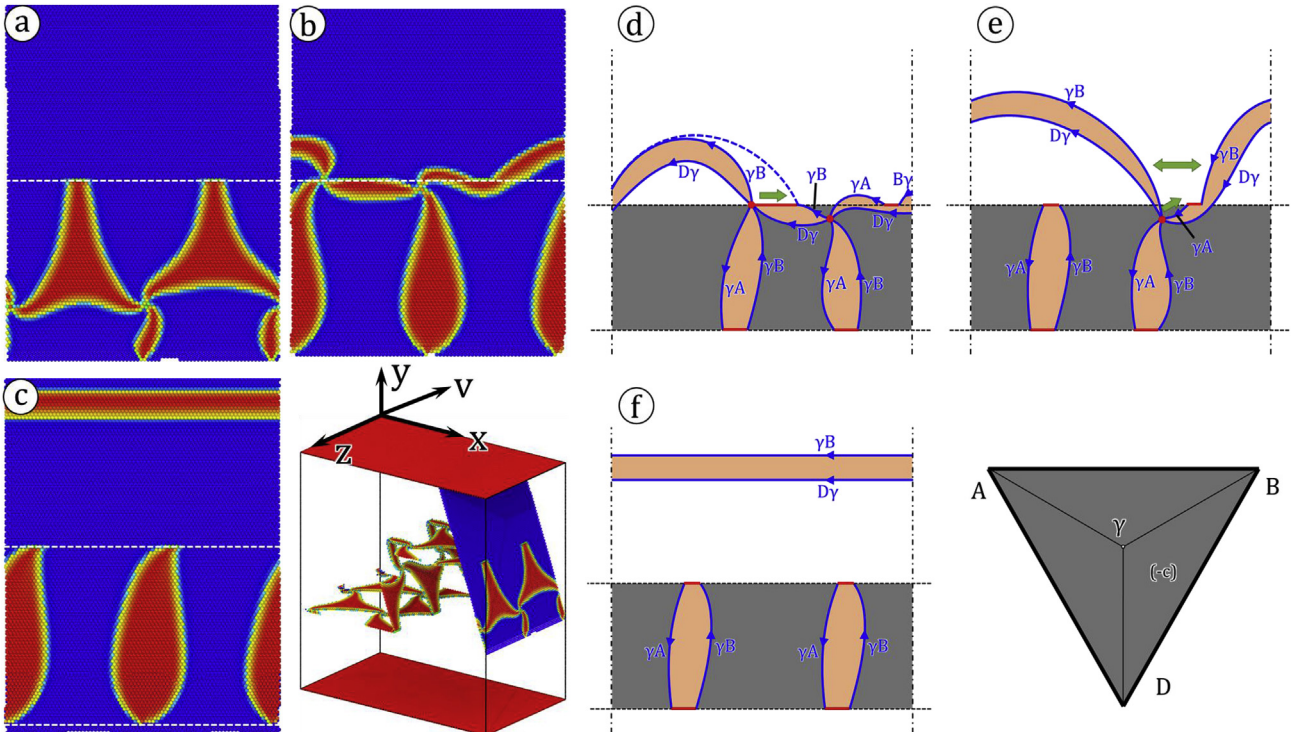


**Fig. 10.** Emission of lattice dislocation from the facets of a Case II disconnection under compressive loading. (a–c): Snapshots of atomic plane aligning with the facet at various stage of the emission process. The relative orientation of this plane with respect to the bilayer model is shown in the accompanying inset. Atoms are colored by the centro-symmetry parameter (CSP), with blue representing CSP = 0 and red representing CSP = 6. (d–f): Dislocation structure characterized by disregistry analyses. Orientation of all two-dimensional representations follows the (-c) plane of the Thompson's tetrahedron shown on the bottom right. (For interpretation of the references to color in this figure legend, the reader is referred to the Web version of this article.)

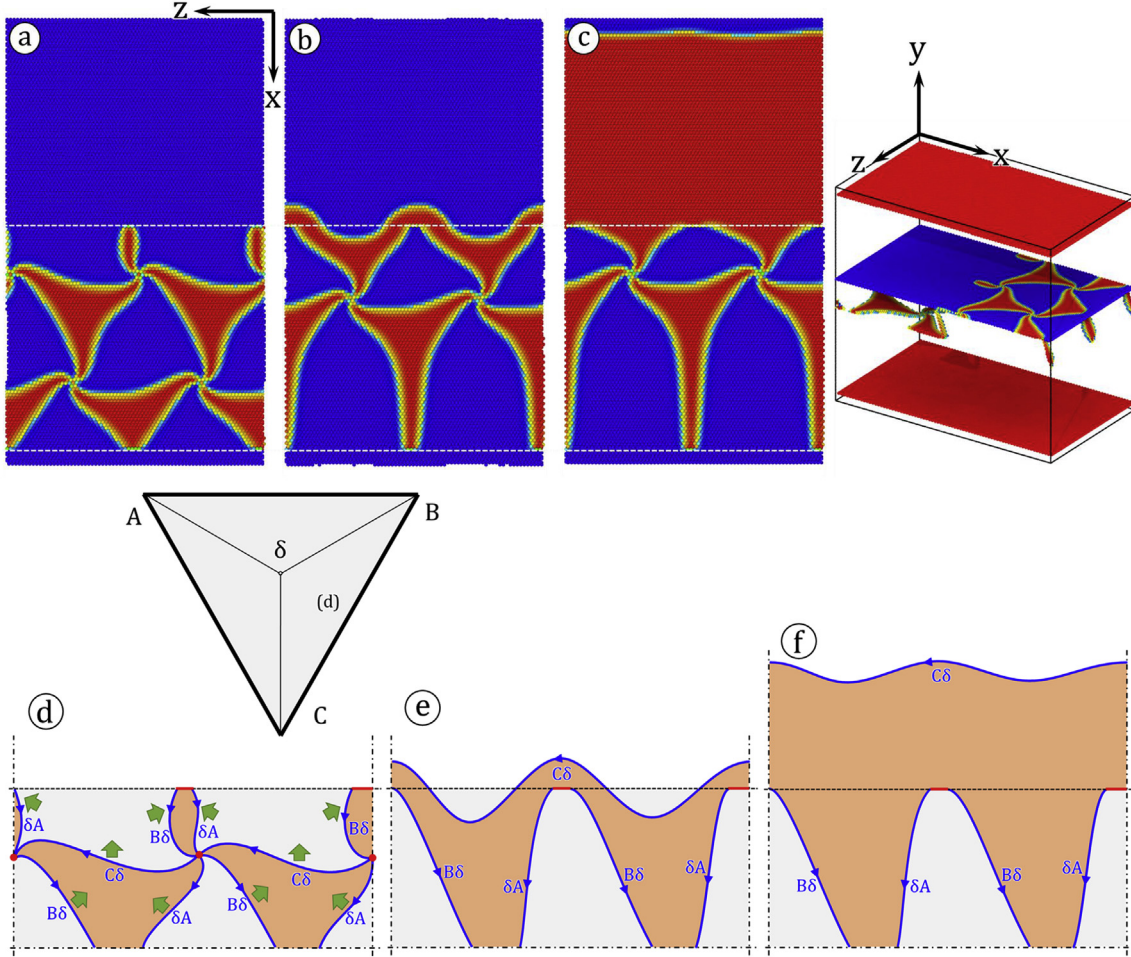


**Fig. 11.** Emission of lattice dislocation from the facet of a (111) interface under a shear stress  $\sigma_{yx} > 0$ . (a–c) show the snapshots of the atomic plane as indicated on the image on the top right. (d–f) show detailed dislocation structures characterized from disregistry analysis.

reside are shown in plan-view (Fig. 11a–c). The viewing direction is along  $-y$ . Dislocation structures, as characterized by disregistry analyses, have been shown in Fig. 11d–f. Details on the disregistry analyses are shown in the Suppl. Mater. Section 3. On the facet of interface, MDN with pure edge dislocations exist. The Burgers vectors of all the partials are either parallel to or have a significant component in the shear loading direction. Under this  $\sigma_{yx}$ ,  $C\delta$  partials are driven along the  $-x$  direction. While the  $B\delta$  and  $\delta A$  partials are driven into each other in such a way that the area of the stacking faults is reduced. The net force felt by each partial dislocation is schematically marked in Fig. 11d using green arrows. Under these forces, the  $C\delta$  partial moves along  $C\delta$  direction and the dislocation nodes (red dots in Fig. 11d) moves and reacts with the stair-rod dislocations (short red line segments in Fig. 11d). The resulting dislocation junction then re-dissociates into a greek-greek/roman-roman type stair-rod and the partial  $C\delta$  (Fig. 11e). At a stress level that is sufficiently high, the partial  $C\delta$  fully emit into Cu, leaving a stacking fault behind (Fig. 11f). In principle, this emission process only needs to overcome an energy barrier set forth by the additional stacking fault energy, as well as the changes dislocation line energy due to changes in the elastic moduli from interface to Cu. The resolved shear stress required for this process is expected to be lower than the mechanisms depicted by Figs. 9 and 10, where significant dislocation bowing is also required.

When  $\sigma_{yx} < 0$ , the dislocation emission mechanism is identical to that of the disconnection 2 under compression, which is depicted

in Fig. 10. The step-by-step process shown by the snap shots of the top interface plane is given in Fig. 12. The plan views (Fig. 12a–c) are along the viewing direction of  $-y$ . Corresponding dislocation structures have been characterized by disregistry analyses and have been presented in Fig. 12d–f. As seen, the main distinction of the current mechanism from the one active when  $\sigma_{yx} > 0$  is the emission of a perfect dislocation, instead of a single Shockley partial. The emitted trailing partial dislocation,  $C\delta$ , feels a much stronger force (twice as strong) due to the applied stress compared with the leading partial,  $B\delta$ , since the former's Burgers vector is perfectly aligned with the loading direction. The emission of  $B\delta$  is therefore due to its resultant force from the applied shear stress as well as the interaction force from partial  $C\delta$ . Similar principles also apply for the mechanisms identified for the facets of disconnections under compression (Figs. 9 and 10). The critical stress for dislocation emission under this mechanism is also expected to be significantly higher than that for the case when  $\sigma_{yx} > 0$ , as the energy barrier of emitting one perfect dislocation is higher than that of only one partial.

### 3.3.3. Strengths of the faceted interfaces under compression and shear

Under compression, the distinct dislocation emission mechanism of Case I disconnection, suggests that the emission process is controlled by the initial bowing of partial dislocations that were initially parallel to the step vectors (schematically shown in Fig. 9f).

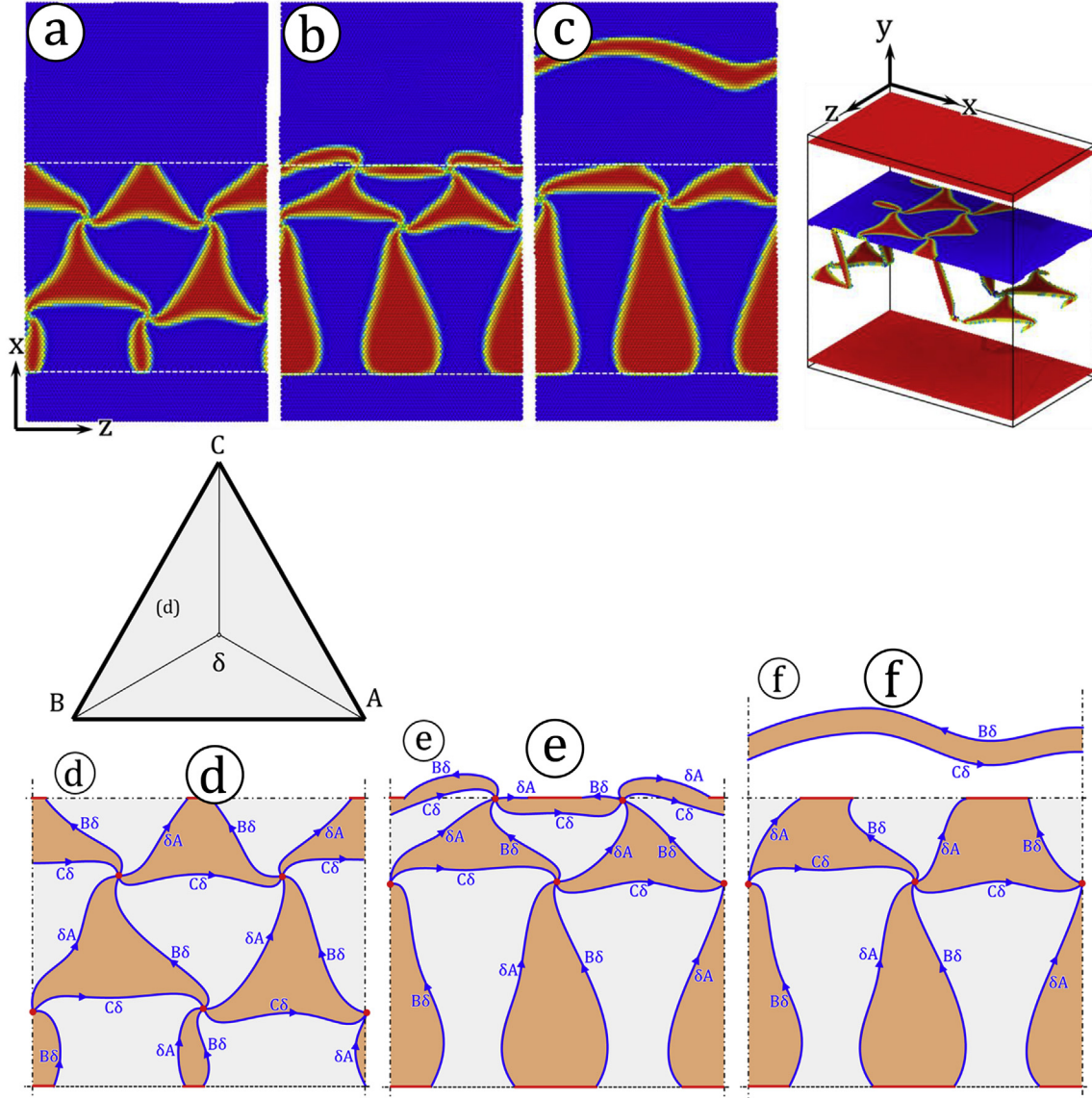


**Fig. 12.** Emission of lattice dislocation from the facets of a Case I disconnection under shear loading, where  $\sigma_{yx} < 0$ . The applied shear stress  $\sigma_{yx}$  is on the x-z plane and along the negative sense of the x axis. (a–c) show the snapshots of the atomic plane as indicated on the image on the right hand side. (d–f) show the dislocation structures characterized by disregistry analysis.

Therefore, compressive strength<sup>4</sup> of the interfaces are inversely related to the magnitude of the step vector  $|\mathbf{l}|$ , and thus to the disconnection height  $h$ . Under isotropic assumptions, the critical compressive stress to bow these partial dislocations to radius  $|\mathbf{l}|/2$ , or  $h/2\sin(70.5^\circ)$  is

$$\sigma_{comp} = \sigma_0 + \frac{m\bar{\mu}\bar{b}}{|\mathbf{l}|} = \sigma_0 + \frac{n\bar{\mu}\bar{b}}{h} \quad (6)$$

where  $m$  and  $n$  are constants accounting for the line tension of the dislocations under various radii of curvature, Schmidt factor, relation between  $|\mathbf{l}|/2$  and  $h/2$ , etc.,  $\bar{b}$  is the effective magnitude of Burgers vectors of interfacial partial dislocations, and  $\sigma_0$  is a constant stress corresponding to the compressive strength of a hypothetical Case I disconnection with  $h \rightarrow \infty$ . As shown in Fig. 13, the

compressive strength indeed obeys Eqn. (6) in Case I. A curve fit with  $\sigma_0 = 3.61$  GPa,  $n = 9.03$ ,  $\bar{\mu} = 62$  GPa and  $\bar{b} = 1.46$  Å has been provided in Fig. 13 as the dash-dotted line. Under very small values of  $h$ , the required  $\sigma_{comp}$  is so high that another dislocation nucleation mechanism from dislocation nodes of the MDN is activated [54]. This mechanism, which corresponds to a compressive strength of ~10 GPa, deviates the measured compressive strength from the inverse power law (Fig. 13). Dislocation emission for Cases II and III do not require the initially confined bowing of partial dislocations as a function of disconnection height, which is reflected in Fig. 13 as the flat features within the Cases II and III.

On the other hand, characteristic strength levels seem to exist for each case. For Case I, at its minimum, the strength of the interface is ~5 GPa; for Case II, it is relatively constant ~3.8 GPa; for Case III, it is ~2.8 GPa. The compressive strength appears to drop significantly at the boundaries between cases. This behavior is ascribed to the different dislocation structures on the facets of the disconnections. As shown in Fig. 4, going from Case I to III, the total

<sup>4</sup> Critical stress for the emission of the first dislocation(s).

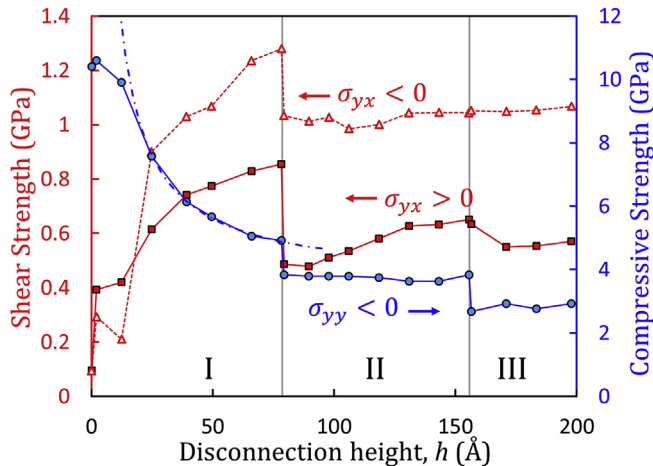


**Fig. 13.** Shear and compressive strengths of terraced interfaces as a function of the disconnection height, or facet size. These strengths are defined as the critical stress for the emission of the first lattice dislocation(s).

number of dislocations with line directions parallel/antiparallel to AB direction increases. Under applied compression, the RSS drives the networks of dislocations towards one edge of facets, as noted in Figs. 10–12. Similar to a scenario of dislocations' pile-up at grain boundaries, dislocations on the facets also piles up at the edges of disconnections. The mechanical advantage provided by the dislocation pile-ups essentially governs the strength of the interfaces for Cases II and III. It can further be inferred that with additional increase in the case number and additional dislocations added to the facets, compressive strength would further reduce.

Under shear loading, the strength of the interfaces is substantially smaller than that under compression. This, in part, is due to the striking difference in the maximum Schmidt factor between the two loading conditions, i.e.  $S_{\text{Shear}} = 1.00$  vs.  $S_{\text{Comp.}} = 0.33$ . This can be verified by comparing the compressive strength for Case III, ~2.8 GPa, and the shear strength when  $\sigma_{yx} < 0$ , ~1 GPa. This comparison is meaningful as the dislocation structures on the facets of disconnections are identical to the ones on the facets of interface. The interfacial shear strengths under both loading directions rapidly increases as the Case I disconnection height increases. At the onset of Case II, substantial drops of shear strength (0.25 GPa for  $\sigma_{yx} < 0$  and 0.37 GPa for  $\sigma_{yx} > 0$ ) occur. After the initial drop, subsequent trends of variations in shear strengths are less discernible, if any. In addition, as predicted in Section 3.3.2, the overall shear strength of the interface under  $\sigma_{yx} < 0$  is greater than under  $\sigma_{yx} > 0$ .

The initial increase, as a function of the disconnection height, in the interface shear strength demonstrated by Case I disconnections can be ascribed to the existence of the residual stresses as variation in the Burgers vectors in the disconnections (Fig. 7i-p shows the variation in the residual shear strains). These residual strains can be as high as 0.0075 near the facets of the disconnection, which, estimated by Cu's shear modulus of 48 GPa, correspond to a residual shear stress of  $\sigma_{yx} = \pm 0.36$  GPa. The emission of dislocations would need to overcome this stress inhomogeneity, therefore, for Case I disconnections, the interfacial shear strength increases with the increase of disconnection height and Burgers vector (see the red hollow triangles and red filled squares in Fig. 13). At the boundary between Cases I and II, the stress inhomogeneity was removed (compare Fig. 7k and l), this strengthening effect due to the build-up of Burgers vector in the disconnection was removed. Note that the stresses drop by 0.2–0.4 GPa. In addition, in Cases II and III, networks of MDNs form on the facets of disconnections, and, under the RSS due to the applied shear loading, are forced to the edges at

which emissions of dislocations occur. In these cases, the interaction between the dislocations on the facets of disconnections and those on the facets of interface cannot be overlooked. In fact, as explained in the Suppl. Mater. Section S4 with help of Nabarro's interaction equations [52,55], the  $\gamma D$  type of edge partials on the facet planes tend to facilitate the emission process. Under the influence of this dislocation-dislocation interaction, the strengthening effect due to the stress inhomogeneity breaks down and the strength variation after the initial drop becomes less significant with increasing disconnection height.

#### 4. Discussion

This work is concerned with the interfacial facets. Using the concept of super disconnections, this work sheds light on structure, energy, and mechanical properties of interfacial facets. While generality was maintained throughout the analyses of our results, the applicability and limitations of our findings need to be formally discussed.

##### 4.1. Relevance between modeled geometries with reality

First, it is apparent that the terraced interface considered in this work resemble a "step-terrace-step" configuration rather than the well-known "hill-and-valley" geometry (see Fig. 2). This model construct was specifically adopted so that the various effects of facet size can be captured without substantially changing the size of the simulation box. Indeed, this construct insures that the asymptotic normal of the interface is [111]. When the size of the  $(\bar{1}\bar{1}1)$  and  $(1\bar{1}\bar{1})$  facets are varied, the simulation box would only vary in the y dimension. In contrast, if the classical "hill-and-valley geometry" was adopted, the asymptotic interface normal would deviate from [111]. Two complexities would result: (1) a periodic box with admissible strains—in x and z direction may be too large, (2) variation of facet size would result in dimensional change, not only in y direction (to eliminate boundary effects), but also in the x direction (if the step vectors fall within the x-y plane). While this work only considered the size effect on the inclined facets (Disconnections 1 and 2 shown in Fig. 2), a similar size effect on the "horizontal" facets of the interface also exists. In fact, one could easily show that the underlying mechanism for the size effect herein shares the same root as the one we have discussed in our original submission. Due to this very reason, we intentionally neglected this length scale effect. The choice of the x-dimension of our simulation cell ensures that the two "horizontal" facets have near-zero Burgers vectors, when treated as disconnections.

Second, the facets modeled in this work are of the special, {111} type. Other low-index facets, such as the {100} and {110} types have not been investigated in this work. A generalized interface between two FCC crystals may contain facets of the {100} {110} and {111} type. Also, terraced interfaces between two dissimilar crystals, such FCC-BCC, BCC-HCP, etc., have not been considered. Due to our choice of the facets, the step vectors on both adjoining surfaces are parallel/anti-parallel to the {112} direction. The resulting possible Burgers vectors of the disconnections, therefore, are also parallel/anti-parallel to the step vectors. This choice of special case of interfacial super disconnections simplified the analyses involved in this work. However, we expect that the principles that have been discovered in this work, i.e. the effects of size, coherency, dislocation structure, and Burgers vector on a facet, would be generally applicable to a broad range of facet types. In addition, this work puts forward a methodology on the analyses of more complex facets, which involved the disclination characters, i.e. with out-of-facet Burgers vectors.

#### 4.2. Original understanding gained towards the structural, energetic and mechanical properties of terraced interfaces

This work demonstrates that the structures of the interfacial disconnections are composed of basic building blocks of a regular flat interface, namely MDN, coherent regions, and dislocation nodes. The edges of the disconnections comprise stair-rod dislocations of the acute and obtuse types, which connects the stacking faults on two adjoining facet planes. The coherent regions on two connecting facet planes join by the coherent step corners. Although these coherent corners are associated with excess energies, the formal treatment of which is beyond the scope of this work. Instead, this work sums this energy contribution with the interfaces' chemical energy, core energy and near-field coherency energy and explicitly evaluated the effect of the Burgers vector of disconnections on the energy-structure-property correlation. It was shown that these inherent energy components dominate the specific energy ( $\gamma_{\text{Spec}}$ ) of an interface, with relatively small influenced from the disconnection's Burgers vector. Nonetheless, it was also shown in this work that the Burgers vector contributes to the total energy of the disconnections in a manner similar to that of a dislocation. A clear quadratic relation between the excess interfacial strain energy and the Burgers vector of a disconnection can be seen.

Mechanisms by which dislocations are emitted from interfaces have also been carefully analyzed. These mechanisms were found to depend on not only the loading conditions, but also on the specific dislocation structure of the super disconnections. For instance, emission of dislocations from Case I disconnections under compression requires the lateral bowing of the partial interfacial dislocations and a subsequent nucleation of a dislocation loop with Burgers vector along the step vector of the disconnection. Emission of dislocations from Case II disconnections under compression requires the combination of dislocation nodes with stair-rod dislocations, forming complex junctions, and the subsequent dissociation of dislocations from said junctions. Under compressive loading, the applied compressive state of stress is resolved into the facet planes as shear stress, which activates the motion of dislocations therein.

As the dislocation structure of the facets of disconnections can be similar to facets of the interface, commonalities also exist in the dislocation emission mechanism between the flat interfaces and the facets. Under shear loading, the specific emission mechanisms are dependent on the loading direction with respect to the disconnections. Two mechanisms can be active. The first mechanism is identical to the one active for Case II disconnections under compression. Both mechanisms involve the formation of junctions between dislocation nodes and stair-rod dislocations, and the subsequent dissociation of these junctions.

It is important to note that the mass-conserving dislocation operations to emit a dislocation are non-unique, although the aforementioned critical events, namely dislocation bowing, combination/dissociation between a dislocation node with stair-rod dislocations, are necessary. For instance, in the [Supplemental Materials Section S5](#), we have provided several possible alternative mechanisms to the ones identified for dislocation emission from facets under compression ([Fig. 9](#)). It is apparent that these mechanisms can operate at a much smaller spatial period and is therefore permissible in a smaller simulation cell. Since these mechanisms correspond to a much smaller bowing radius for a given dislocation, the corresponding emission stress is likely to be higher, vice versa. Therefore, caution must be given to the obtained stress values as they may be very much dependent on the size of the simulation cell.

The obtained shear and compressive strengths of the faceted

interface correspond to the first event of dislocations' emission, which were shown to strongly depend on the dislocation structure and Burgers vector of the disconnections. It was found that the compressive strength for interfaces with Case I disconnections is inversely related to the height—therefore Burgers vector—of the disconnections. With each increase in the case number, which is associated in the increase in the net Burgers vector in the MDN on the facets, the compressive strength exhibits a clear reduction. Pile-up of MDN at the edge of facets was found to have contributed to such behavior. The shear strength of interfaces with Case I disconnections was shown to increase with increasing height, which has been ascribed to the increasingly heterogeneous stress distribution associated with the increasing Burgers vector. For Cases II and III disconnections, the emission of dislocations under shear loading are influenced strongly by the presence of parallel dislocations on the neighboring facets. Therefore, the variation in strength is less significant.

In this work, although we report the shear and compressive strengths of the faceted interfaces, the precise values should not be directly compared with experiments. Indeed, the emission of dislocations are thermally activated [52,56] and strongly dependent on strain rate and temperature. In this work, we make no attempt to predict the precise critical stress for the emission of dislocations under compression and shear. Instead, we emphasize the lateral comparison on the impact of dislocations, with their height, dislocation structure and Burgers vector as variables, on the associated strength of interfaces.

#### 4.3. Technical implications of the present work

Due to the presence of MDNs, typical semi-coherent interfaces possess relatively low resistance to shear compared to the adjoining materials' theoretical shear strengths [12,46,57–61]. Typical shear strengths of interfaces are: around 0.5 GPa for Cu-Nb interfaces [12,57,58], 0.8 GPa if the Cu-Nb interfaces are Kr + ion implanted [59], ~1.0 GPa for Mg-Nb interfaces [61], ~0.6 GPa for Cu-CrN interfaces [46]. The reduced shear strength increases the resistance to slip transmission across an interface by promoting core-spreading of an incoming gliding dislocation [62–64], thereby increasing the strength of a material with interfaces engineered parallel or perpendicular to the loading direction [50,62,65]. However, such "weak interfaces" may reduce materials' overall strength if substantial resolve shear stress exists on the interface plane, which, in turn, may lead to strong mechanical anisotropy.

Terraced interfaces appear to improve an interface's overall resistance to shear, while not substantially raising the localized shear strength to maintain core-spreading of incoming dislocations. For instance, the ARB induced, mechanically stabilized Cu-Nb interfaces have been shown to contain the classic 'hill and valley' structure along a compact direction [11,23,66]. These interfaces have markedly higher peak shear strength (~1.8 GPa) as compared to their flat counter parts, when loaded perpendicular to the 'hills and valleys' [2]. Recent atomistic investigations on this matter suggest that, by engineering interfacial facets onto flat Cu-Nb interfaces, their shear resistance can be improved by 0.3–0.8 GPa [45]. These instances indicate that immense design space may exist for terraced semi-coherent interfaces with tailored shear characteristics by means of interfacial morphology control. Indeed, present findings suggest that, due to the variation of their Burgers vector, the preferred size of facets (at least those without a disclination character) on a terraced interface, might be quantized. In addition, the critical stress for dislocation emission from facets is strongly dependent on their size as well.

Besides the severe plastic deformation processes, such as ARB, routes for fabrication of materials with intentionally terraced

interfaces may include thin film growth with/without surface roughening by ion bombardment. For instance, due to their lattice mismatch, growth of Ge thin film on a Si substrate has been shown to proceed via the Stranski-Krastanov growth mode, i.e. an initial, uniform growth for several atomic monolayers followed by growth of non-flat nano-hut clusters, then transitioning to large 3D islands [67]. Another example of similar nature is offered by hetero-epitaxial growth of AlN on Si(111) [68]. In this case, the large lattice mismatch led to growth of wurtzitic AlN in the Volmer-Weber island growth mode from the beginning, leading to a rough AlN top surface [69]. Subsequent growth of dissimilar materials on the rough surfaces then results in terraced interface. In addition to growth induced roughening, surface roughening by ion bombardment has long been known and studied, from ion induced pattern formation on amorphous surfaces [70] to ion induced roughening on surfaces of polycrystalline metal thin films [71]. Ion beam roughened surfaces offer growth templates on top of which new growth would adopt different surface morphologies [72], thereby offering an additional avenue for engineering interfaces with intentional roughness.

## 5. Conclusions

In this work, using atomistic simulations, the energetic, structural and mechanical characteristics of terraced Cu-Ni {111} semi-coherent interfaces have been systematically analyzed by treating the facets as interfacial super disconnections. It was found that the dislocation character of a facet periodically emerges and disappears as a function of its size, corresponding to the periodic changes in its specific energy. In addition, the dislocation structure on a facet also changes as its length increases, which is associated with the quantized changes in coherency along the step vectors. The mechanical response of a faceted interface has also been shown to greatly depend on the facet size, which is manifested by the dependence of dislocation emission mechanism on a facet's dislocation structure, and the dependence of dislocation emission stresses on both the facet's Burgers vector and dislocation structure.

## Acknowledgement

The authors gratefully acknowledge partial project support from the U.S. National Science Foundation (NSF OIA-1541079). SS also acknowledges the support provided by the LSU Office of Research and Economic Development and the Department of Mechanical and Industrial Engineering. Portions of this research were conducted with high performance computing resources provided by Louisiana State University (<http://www.hpc.lsu.edu>).

## Appendix A. Supplementary data

Supplementary data to this article can be found online at <https://doi.org/10.1016/j.actamat.2019.04.016>.

## References

- [1] J.S. Carpenter, S.C. Vogel, J.E. Ledonne, D.L. Hammon, I.J. Beyerlein, N.A. Mara, Bulk texture evolution of Cu-Nb nanolamellar composites during accumulative roll bonding, *Acta Mater.* 60 (2012) 1576–1586, <https://doi.org/10.1016/j.actamat.2011.11.045>.
- [2] J. Wang, K. Kang, R.F. Zhang, S.J. Zheng, I.J. Beyerlein, N.A. Mara, Structure and property of interfaces in ARB Cu/Nb laminated composites, *JOM* 64 (2012) 1208–1217, <https://doi.org/10.1007/s11837-012-0429-7>.
- [3] S. Zheng, I.J. Beyerlein, J.S. Carpenter, K. Kang, J. Wang, W. Han, N.A. Mara, High-strength and thermally stable bulk nanolayered composites due to twin-induced interfaces, *Nat. Commun.* 4 (2013), <https://doi.org/10.1038/ncomms2651>.
- [4] J. Wang, L. Liu, C.N. Tomé, S.X. Mao, S.K. Gong, Twinning and de-twinning via glide and climb of twinning dislocations along serrated coherent twin boundaries in hexagonal-close-packed metals, *Mater. Res. Lett.* 1 (2013) 81–88, <https://doi.org/10.1080/21663831.2013.779601>.
- [5] A. Kumar, J. Wang, C.N. Tomé, First-principles study of energy and atomic solubility of twinning-associated boundaries in hexagonal metals, *Acta Mater.* 85 (2015) 144–154, <https://doi.org/10.1016/j.actamat.2014.11.015>.
- [6] J.F. Nie, Y.M. Zhu, J.Z. Liu, X.Y. Fang, Periodic segregation of solute atoms in fully coherent twin boundaries, *Science* 340 (80–) (2013) 957–960, <https://doi.org/10.1126/science.1229369>.
- [7] C.H. Liebscher, A. Stoffers, M. Alam, L. Lymparakis, O. Cojocaru-Mirédin, B. Gault, J. Neugebauer, G. Dehm, C. Scheu, D. Raabe, Strain-induced asymmetric line segregation at faceted Si grain boundaries, *Phys. Rev. Lett.* 121 (2018), 015702, <https://doi.org/10.1103/PhysRevLett.121.015702>.
- [8] N.J. Peter, T. Frolov, M.J. Duarte, R. Hadian, C. Ophus, C. Kirchlechner, C.H. Liebscher, G. Dehm, Segregation-induced nanofaceting transition at an asymmetric tilt grain boundary in copper, *Phys. Rev. Lett.* 121 (2018) 255502, <https://doi.org/10.1103/PhysRevLett.121.255502>.
- [9] N.A. Mara, N. Li, A. Misra, J. Wang, Interface-driven plasticity in metal–ceramic nanolayered composites: direct validation of multiscale deformation modeling via *in situ* indentation in TEM, *JOM* 68 (2016) 143–150, <https://doi.org/10.1007/s11837-015-1542-1>.
- [10] S. Shao, J. Wang, A. Misra, R.G. Hoagland, Spiral patterns of dislocations at nodes in (111) semi-coherent FCC interfaces, *Sci. Rep.* 3 (2013) 2448, <https://doi.org/10.1038/srep02448>.
- [11] J. Wang, C. Zhou, I.J.J. Beyerlein, S. Shao, Modeling interface-dominated mechanical behavior of nanolayered crystalline composites, *JOM* 66 (2014) 102–113, <https://doi.org/10.1007/s11837-013-0808-8>.
- [12] J. Wang, R.G. Hoagland, J.P. Hirth, A. Misra, Atomistic simulations of the shear strength and sliding mechanisms of copper–niobium interfaces, *Acta Mater.* 56 (2008) 3109–3119, <https://doi.org/10.1016/j.actamat.2008.03.003>.
- [13] C. Herring, Some theorems on the free energies of crystal surfaces, *Phys. Rev. E* 82 (1951) 87–93, <https://doi.org/10.1103/PhysRev.82.87>.
- [14] S.J. Watson, Emergent parabolic scaling of nano-faceting crystal growth, *Proc. R. Soc. A Math. Phys. Eng. Sci.* 471 (2014), 20140560, <https://doi.org/10.1098/rspa.2014.0560>.
- [15] T. Hsieh, R. Balluffi, Observations of roughening/de-faceting phase transitions in grain boundaries, *Acta Metall.* 37 (1989) 2133–2139, [https://doi.org/10.1016/0001-6160\(89\)90138-7](https://doi.org/10.1016/0001-6160(89)90138-7).
- [16] J.C. Hamilton, D.J. Siegel, I. Daruka, F. Léonard, Why do grain boundaries exhibit finite facet lengths? *Phys. Rev. Lett.* (2003), 246102 <https://doi.org/10.1103/PhysRevLett.90.246102>.
- [17] B. Runnels, I.J. Beyerlein, S. Conti, M. Ortiz, A relaxation method for the energy and morphology of grain boundaries and interfaces, *J. Mech. Phys. Solids* 94 (2016) 388–408, <https://doi.org/10.1016/j.jmps.2015.11.007>.
- [18] J.P. Hirth, Dislocations, steps and disconnections at interfaces, *J. Phys. Chem. Solids* 55 (1994) 985–989, [https://doi.org/10.1016/0022-3697\(94\)90118-X](https://doi.org/10.1016/0022-3697(94)90118-X).
- [19] J.P. Hirth, R. Pond, Steps, dislocations and disconnections as interface defects relating to structure and phase transformations, *Acta Mater.* 44 (1996) 4749–4763.
- [20] J.P. Hirth, R.C. Pond, R.G. Hoagland, X.-Y. Liu, J. Wang, Interface defects, reference spaces and the Frank–Bilby equation, *Prog. Mater. Sci.* 58 (2013) 749–823, <https://doi.org/10.1016/j.pmatsci.2012.10.002>.
- [21] D.M. Barnett, J. Lothe, An image force theorem for dislocations in anisotropic bicrystals, *J. Phys. F Met. Phys.* 4 (1974) 1618–1635, <https://doi.org/10.1088/0305-4608/4/10/010>.
- [22] Z. Suo, Singularities, interfaces and cracks in dissimilar anisotropic media, *Proc. R. Soc. A Math. Phys. Eng. Sci.* 427 (1990) 331–358, <https://doi.org/10.1098/rspa.1990.0016>.
- [23] J. Wang, Q. Zhou, S. Shao, A. Misra, Strength and plasticity of nanolaminated materials, *Mater. Res. Lett.* 5 (1) (2017) 1–19, <https://doi.org/10.1080/21663831.2016.1225321>.
- [24] S. Shao, F. Akasheh, J. Wang, Y. Liu, Alternative misfit dislocations pattern in semi-coherent FCC {100} interfaces, *Acta Mater.* 144 (2018) 177–186, <https://doi.org/10.1016/j.actamat.2017.10.052>.
- [25] H. Long, H. Wei, Y. Liu, S. Mao, J. Zhang, S. Xiang, Y. Chen, W. Gui, Q. Li, Z. Zhang, X. Han, Effect of lattice misfit on the evolution of the dislocation structure in Ni-based single crystal superalloys during thermal exposure, *Acta Mater.* 120 (2016) 95–107, <https://doi.org/10.1016/j.actamat.2016.08.035>.
- [26] R.D. Field, T.M. Pollock, W.H. Murphy, The development of  $\gamma/\gamma'$  interfacial dislocation networks during creep in Ni-base superalloys, in: *Superalloys 1992 Seventh Int. Symp.*, 1992, pp. 557–566, [https://doi.org/10.7449/1992\\_Superalloys\\_1992\\_557\\_566](https://doi.org/10.7449/1992_Superalloys_1992_557_566). TMS.
- [27] H. Gabrisch, D. Mukherji, R.P. Wahi, Deformation-induced dislocation networks at the  $\gamma/\gamma'$  interfaces in the single-crystal superalloy SC16: a mechanism-based analysis, *Philos. Mag. A* 74 (1996) 229–249, <https://doi.org/10.1080/01418619608239699>.
- [28] C. Carry, J. Strudel, Apparent and effective creep parameters in single crystals of a nickel base superalloy-II. Secondary creep, *Acta Metall.* 26 (1978) 859–870, [https://doi.org/10.1016/0001-6160\(78\)90035-4](https://doi.org/10.1016/0001-6160(78)90035-4).
- [29] A.K. Singh, N. Louat, K. Sadananda, Dislocation network formation and coherency loss around gamma-prime precipitates in a nickel-base superalloy, *Metall. Trans. A* 19 (1988) 2965–2973, <https://doi.org/10.1007/BF02647723>.
- [30] S. Zheng, S. Shao, J. Zhang, Y. Wang, M.J. Demkowicz, I.J. Beyerlein, N.A. Mara, Adhesion of voids to bimetal interfaces with non-uniform energies, *Sci. Rep.* 5

- (2015), 15428, <https://doi.org/10.1038/srep15428>.
- [31] S.J. Zheng, J. Wang, J.S. Carpenter, W.M. Mook, P.O. Dickerson, N.A. Mara, I.J. Beyerlein, Plastic instability mechanisms in bimetallic nanolayered composites, *Acta Mater.* 79 (2014) 282–291, <https://doi.org/10.1016/j.actamat.2014.07.017>.
- [32] J. Wang, A. Misra, An overview of interface-dominated deformation mechanisms in metallic multilayers, *Curr. Opin. Solid State Mater. Sci.* 15 (2011) 20–28, <https://doi.org/10.1016/j.cossms.2010.09.002>.
- [33] R.F. Zhang, J. Wang, I.J. Beyerlein, a. Misra, T.C. Germann, Atomic-scale study of nucleation of dislocations from fcc–bcc interfaces, *Acta Mater.* 60 (2012) 2855–2865, <https://doi.org/10.1016/j.actamat.2012.01.050>.
- [34] N.A. Mara, D. Bhattacharyya, P. Dickerson, J.K. Baldwin, R.G. Hoagland, A. Misra, *Metallic Nanolayered Composites Exhibit Ultra-high Strength and Ductility*, 2008, pp. 8–9.
- [35] N.A. Mara, D. Bhattacharyya, R.G. Hoagland, A. Misra, Tensile behavior of 40 nm Cu/Nb nanoscale multilayers, *Scripta Mater.* 58 (2008) 874–877, <https://doi.org/10.1016/j.scriptamat.2008.01.005>.
- [36] A. Misra, R.G. Hoagland, H. Kung, Thermal stability of self-supported nanolayered Cu/Nb films, *Philos. Mag. A* 84 (2004) 1021–1028, <https://doi.org/10.1080/14786430310001659480>.
- [37] A. Misra, X. Zhang, D. Hammon, R.G. Hoagland, Work hardening in rolled nanolayered metallic composites, *Acta Mater.* 53 (2005) 221–226, <https://doi.org/10.1016/j.actamat.2004.09.018>.
- [38] A. Misra, J.P. Hirth, R.G. Hoagland, Length-scale-dependent deformation mechanisms in incoherent metallic multilayered composites, *Acta Mater.* 53 (2005) 4817–4824, <https://doi.org/10.1016/j.actamat.2005.06.025>.
- [39] S. Plimpton, Fast parallel algorithms for short-range molecular dynamics, *J. Comput. Phys.* 117 (1995) 1–19, <https://doi.org/10.1006/jcph.1995.1039>.
- [40] B. Onat, S. Durukanoğlu, An optimized interatomic potential for Cu–Ni alloys with the embedded-atom method, *J. Phys. Condens. Matter* 24 (2014), 035404, <https://doi.org/10.1088/0953-8984/26/3/035404>.
- [41] M.S. Daw, M.I. Baskes, Embedded-atom method: derivation and application to impurities, surfaces, and other defects in metals, *Phys. Rev. B* 29 (1984) 6443–6453, <https://doi.org/10.1103/PhysRevB.29.6443>.
- [42] M. Daw, M. Baskes, Semiempirical, Quantum mechanical calculation of hydrogen embrittlement in metals, *Phys. Rev. Lett.* 50 (1983) 1285–1288, <https://doi.org/10.1103/PhysRevLett.50.1285>.
- [43] S. Shao, J. Wang, A. Misra, Energy minimization mechanisms of semi-coherent interfaces, *J. Appl. Phys.* 116 (2014), 023508, <https://doi.org/10.1063/1.4889927>.
- [44] J. Wang, O. Anderoglu, J.P. Hirth, A. Misra, X. Zhang, Dislocation structures of  $\Sigma 3$  {112} twin boundaries in face centered cubic metals, *Appl. Phys. Lett.* 95 (2009), 021908, <https://doi.org/10.1063/1.3176979>.
- [45] R.F.F. Zhang, I.J.J. Beyerlein, S.J.J. Zheng, S.H.H. Zhang, A. Stukowski, T.C.C. Germann, Manipulating dislocation nucleation and shear resistance of bimetal interfaces by atomic steps, *Acta Mater.* 113 (2016) 194–205, <https://doi.org/10.1016/j.actamat.2016.05.015>.
- [46] X. Zhang, B. Zhang, Y. Mu, S. Shao, C.D. Wick, B.R. Ramachandran, W.J. Meng, Mechanical failure of metal/ceramic interfacial regions under shear loading, *Acta Mater.* 138 (2017) 224–236, <https://doi.org/10.1016/j.actamat.2017.07.053>.
- [47] D. Bhattacharyya, N.A.A. Mara, P. Dickerson, R.G.G. Hoagland, A. Misra, Compressive flow behavior of Al–TiN multilayers at nanometer scale layer thickness, *Acta Mater.* 59 (2011) 3804–3816, <https://doi.org/10.1016/j.actamat.2011.02.036>.
- [48] N. Li, H. Wang, A. Misra, J. Wang, In situ nanoindentation study of plastic co-deformation in Al–TiN nanocomposites, *Sci. Rep.* 4 (2014) 6633, <https://doi.org/10.1038/srep06633>.
- [49] H.C. Barshilia, K.S. Rajam, Characterization of Cu/Ni multilayer coatings by nanoindentation and atomic force microscopy, *Surf. Coatings. Technol.* 155 (2002) 195–202, [https://doi.org/10.1016/S0257-8972\(02\)00008-7](https://doi.org/10.1016/S0257-8972(02)00008-7).
- [50] S. Shao, H.M. Zbib, I.N. Mastorakos, D.F. Bahr, Deformation mechanisms, size effects, and strain hardening in nanoscale metallic multilayers under nano-indentation, *J. Appl. Phys.* 112 (2012), 044307, <https://doi.org/10.1063/1.4748149>.
- [51] N. Thompson, Dislocation nodes in face-centred cubic lattices, *Proc. Phys. Soc. B* 66 (1953) 481–492, <https://doi.org/10.1088/0370-1301/66/6/304>.
- [52] J.P. Hirth, J. Lothe, *Theory of Dislocations*, second ed., Krieger Publishing Company, Malabar, FL, 1982.
- [53] S.N.S.N. Medyanik, S. Shao, Strengthening effects of coherent interfaces in nanoscale metallic bilayers, *Comput. Mater. Sci.* 45 (2009) 1129–1133, <https://doi.org/10.1016/j.commatsci.2009.01.013>.
- [54] S. Shao, J. Wang, I.J. Beyerlein, A. Misra, Glide dislocation nucleation from dislocation nodes at semi-coherent {111} Cu–Ni interfaces, *Acta Mater.* 98 (2015) 206–220, <https://doi.org/10.1016/j.actamat.2015.07.044>.
- [55] F.R.N. Nabarro, Mathematical theory of stationary dislocations, *Adv. Phys.* 1 (1952) 269–394, <https://doi.org/10.1080/00018735200101211>.
- [56] S. Shao, A. Misra, H. Huang, J. Wang, Micro-scale modeling of interface-dominated mechanical behavior, *J. Mater. Sci.* 53 (8) (2017) 5546–5561, <https://doi.org/10.1007/s10853-017-1662-9>.
- [57] N.A. Mara, D. Bhattacharyya, J.P. Hirth, P. Dickerson, A. Misra, Mechanism for shear banding in nanolayered composites, *Appl. Phys. Lett.* 97 (2010), 021909, <https://doi.org/10.1063/1.3458000>.
- [58] N. Li, N.A. Mara, J. Wang, P. Dickerson, J.Y. Huang, A. Misra, Ex situ and in situ measurements of the shear strength of interfaces in metallic multilayers, *Scripta Mater.* 67 (2012) 479–482, <https://doi.org/10.1016/j.scriptamat.2012.06.008>.
- [59] S. Mao, S. Özerinç, W.P. King, R.S. Averback, S.J. Dillon, Effect of irradiation damage on the shear strength of Cu–Nb interfaces, *Scripta Mater.* 90–91 (2014) 29–32, <https://doi.org/10.1016/j.scriptamat.2014.07.009>.
- [60] R.W. Hertzberg, R.P. Vinci, J.L. Hertzberg, *Deformation and Fracture Mechanics of Engineering Materials*, fifth ed., Wiley, Hoboken, NJ, 2012.
- [61] S.K. Yadav, S. Shao, Y. Chen, J. Wang, X.-Y. Liu, Atomistic modeling of Mg/Nb interfaces: shear strength and interaction with lattice glide dislocations, *J. Mater. Sci.* 53 (8) (2017) 5733–5744, <https://doi.org/10.1007/s10853-017-1703-4>.
- [62] R.G. Hoagland, R.J. Kurtz, C.H. Henager, Slip resistance of interfaces and the strength of metallic multilayer composites, *Scripta Mater.* 50 (2004) 775–779, <https://doi.org/10.1016/j.scriptamat.2003.11.059>.
- [63] R.G. Hoagland, J.P. Hirth, a. Misra, On the role of weak interfaces in blocking slip in nanoscale layered composites, *Philos. Mag. A* 86 (2006) 3537–3558, <https://doi.org/10.1080/14786430600669790>.
- [64] J. Wang, R.G. Hoagland, J.P. Hirth, a. Misra, Atomistic modeling of the interaction of glide dislocations with “weak” interfaces, *Acta Mater.* 56 (2008) 5685–5693, <https://doi.org/10.1016/j.actamat.2008.07.041>.
- [65] S. Shao, S.N. Medyanik, Interaction of dislocations with incoherent interfaces in nanoscale FCC–BCC metallic bi-layers, *Model. Simulat. Mater. Sci. Eng.* 18 (2010), 055010, <https://doi.org/10.1088/0965-0393/18/5/055010>.
- [66] A.S. Sutton, R.W. Balluffi, *Interfaces in Crystalline Materials*, Oxford University Press, Oxford, 1995.
- [67] Y.W. Mo, D.E. Savage, B.S. Swartzentruber, M.G. Lagally, Kinetic pathway in Stranski-Krastanov growth of Ge on Si(001), *Phys. Rev. Lett.* 65 (1990), 1020, <https://doi.org/10.1103/PhysRevLett.65.1020>.
- [68] W.J. Meng, J. Heremans, Y.T. Cheng, Epitaxial growth of aluminum nitride on Si(111) by reactive sputtering, *Appl. Phys. Lett.* 59 (1991) 2097–2099, <https://doi.org/10.1063/1.106092>.
- [69] W.J. Meng, J. Heremans, Growth of epitaxial aluminum nitride and aluminum nitride/zirconium nitride superlattices on Si(111), *J. Vac. Sci. Technol. A Vacuum, Surfaces, Film* 10 (1992) 1610–1617, <https://doi.org/10.1116/1.578031>.
- [70] A. Keller, S. Fascko, Ion-induced nanoscale ripple patterns on Si surfaces: theory and experiment, *Materials* 3 (10) (2010) 4811–4841, <https://doi.org/10.3390/ma3104811>.
- [71] T. Škeren, K. Temst, W. Vandervorst, A. Vantomme, Ion-induced roughening and ripple formation on polycrystalline metallic films, *New J. Phys.* 15 (2013), 093047, <https://doi.org/10.1088/1367-2630/15/9/093047>.
- [72] A. Roy, K. Bhattacharjee, H.P. Lenka, D.P. Mahapatra, B.N. Dev, Surface roughness of ion-bombarded Si(1 0 0) surfaces: roughening and smoothing with the same roughness exponent, *Nucl. Instrum. Methods Phys. Res. Sect. B Beam Interact. Mater. Atoms* 266 (8) (April 2008) 1276–1281, <https://doi.org/10.1016/j.nimb.2007.10.045>.
- [73] F. Frank, No title, in: *Rep. Symp. Plast. Deform. Cryst. Solids*, Carnegie Institute of Technology, Pittsburgh, PA, 1950.
- [74] B.A. Bilby, No title, in: *Rep. Conf. Defects Cryst. Solids*, London, 1955, p. 124.
- [75] J. Wang, R. Zhang, C. Zhou, I.J. Beyerlein, A. Misra, Characterizing interface dislocations by atomically informed Frank-Bilby theory, *J. Mater. Res.* 28 (2013) 1646–1657, <https://doi.org/10.1557/jmr.2013.34>.
- [76] Y. Chen, S. Shao, X.-Y. Liu, S.K. Yadav, N. Li, N. Mara, J. Wang, Misfit dislocation patterns of Mg–Nb interfaces, *Acta Mater.* 126 (2017) 552–563, <https://doi.org/10.1016/j.actamat.2016.12.041>.